BULLETIN OF THE DRFMC

Theory and Simulation

Département de
Recherche Fondamentale
sur la Matière Condensée

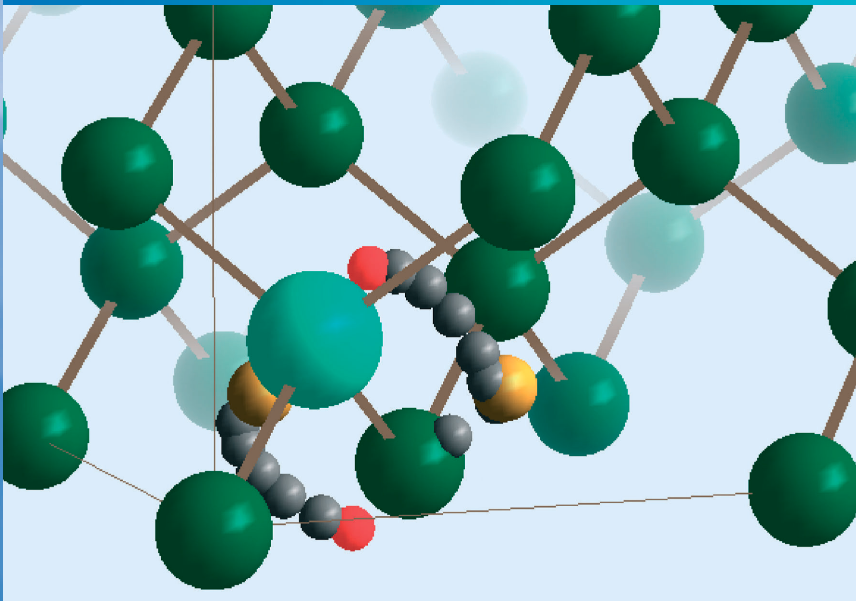

Theory and Simulation

Theory and Simulation

Novembre 2004
n°4

Published by
"Département de Recherche Fondamentale
sur la Matière Condensée"

DRFMC, CEA Grenoble,
17 rue des Martyrs,
F-38054 Grenoble Cedex 9
FRANCE

Chief Editor
Jean-Paul Duraud

Editor
Annie Pesnelle

Scientific Committee
Ariel Brenac, Pierre Dalmas de Réotier,
Olivier Diat, Thierry Douki,
Jean-Paul Duraud, Engin Molva,
Jean-Paul Périn, Annie Pesnelle,
Peter Seyfert, Ricardo Sousa

Layout
Publicum

Photography
Totem de Pierre, CEA

Contact
apesnelle@cea.fr

Foreword

The fourth edition of the Bulletin of the DRFMC (Department of Fundamental Research on Condensed Matter) is dedicated to the theme "Theory and simulation" and contains a description of the activities of the department in this field.

Theory and simulation are connected via statistical physics and constitute an important sector of the research activities on condensed state physics and chemistry. Comparison with experimental data in fact validates models which, in return, enable the behaviour of natural phenomena of the physical world that surrounds us to be predicted or confirmed by computation.

At the DRFMC these activities mainly concern:

- physics of quantum particles in interaction such as heavy fermions, frustration phenomena, quantum magnetism,
- physics of magnetic nano-objects, semiconductors and superconductors,
- physics of surfaces, interfaces and thin films,
- physics of soft matter (polymers, foams),
- quantum chemistry of *f* element complexes,
- physics and chemistry at the interface with biology.

Alongside the study of fundamental subjects, simulation of the behaviour of technological achievements naturally takes its place on account of the department's desire to accompany knowledge transfer to applications.

Finally all these works are backed-up and made possible by the development of simulation methods.

For reasons of editorial convenience, the contributions that illustrate these activities are grouped together according to the organisation of the department, which in a first approach corresponds to a breakdown by theme. I hope that reading this review will enable you to discover the richness of the activities of the department in this field.

Enjoy your reading.

Jean-Paul Duraud
Head of the DRFMC

Contents

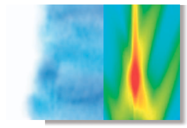

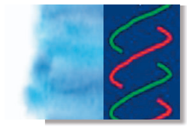

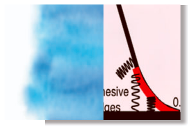

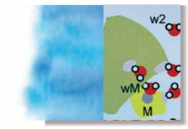
w2
wM
M

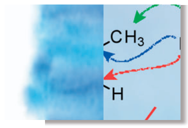
CH3
H


Fe3

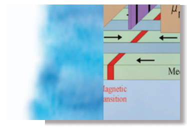

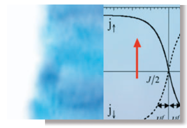

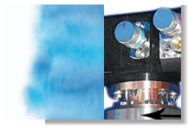

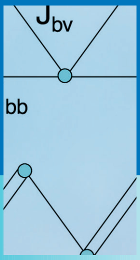

QUASI-1D SPIN CHAINS: FROM THE SAWTOOTH LATTICE TO THE HEISENBERG CHAIN

S. A. Blundell[a]
and M. D. Núñez-Regueiro[b]

a: Service de Physique Statistique, Magnétisme et Supraconductivité (SPSMS), DRFMC
b: Laboratoire de Physique des Solides, Univ. Paris-Sud

Quasi-1D spin chains with a sawtooth shape are studied theoretically. Using an exact diagonalization and extrapolation method, the ground state and low-energy excitations are determined as a function of the different magnetic couplings. Applied to YCuO$_{2.5}$, the method predicts a dispersive spectrum of excitations, with a possibly vanishing gap.

Nous étudions théoriquement des chaînes de spin quasi-unidimensionelles en forme de dent de scie. A partir d'une diagonalisation exacte et d'une extrapolation, nous déterminons l'état fondamental et les excitations de basse énergie en fonction des différents couplages magnétiques. Appliquée à YCuO$_{2.5}$, cette méthode prédit un spectre dispersif des excitations avec un gap pouvant devenir nul.

There is currently great interest in the physics of antiferromagnetic quantum spin systems of reduced dimensionality, such as the one-dimensional spin chains shown in Fig. 1. The simplest example in 1D, shown in Fig. 1a, is the much-studied Heisenberg chain, a linear chain of spins 1/2 in which nearest neighbours are coupled antiferromagnetically. A more recent example is the zigzag spin ladder shown in Fig. 1b.

Here we shall consider another example, the sawtooth or Δ-chain shown in Fig. 1c, which consists of spins 1/2 coupled in a 1D chain of triangles. The Δ-chain has been extensively studied for the case when all spin-spin interactions have equal strength (i.e., when the base-base and base-vertex couplings are equal, $J_{bb} = J_{bv}$). The ground state in this case may be shown to be twofold degenerate. It consists of pairs of spins (one belonging to the base and the other to a neighbouring vertex, as in Fig. 1d) coupled antiferromagnetically to form a spin-singlet state called a *dimer*. The degeneracy arises from the possibility for a base spin to form a dimer either with a spin located on the vertex to its right (R-dimerization) or to its left (L-dimerization). There is also an energy gap to the lowest-energy excitations, which are known as *kinks and antikinks*. A kink (antikink) consists of a domain wall separating a region of R-dimerization on the left (right) from a region of L-dimerization on the right (left). Such domain walls, which separate the system into regions of differing translational symmetry, belong to the general class of *topological* excitations introduced by Shastry and Sutherland more than twenty years ago.

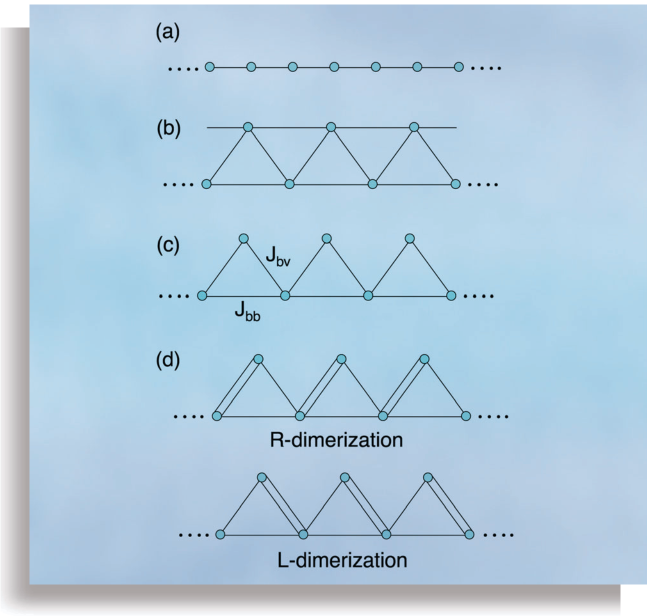

Figure 1: Quasi-1D spin chains: (a) the Heisenberg chain, (b) the zigzag ladder, (c) the sawtooth or Δ-chain. Each site corresponds to a spin 1/2, and single lines indicate an antiferromagnetic Heisenberg coupling of the form $J\, s_i.s_j$ ($J > 0$). (d) shows the two degenerate ground states of the symmetric Δ-chain (where all interactions J are equal), with double lines indicating the formation of a spin-singlet state (or dimer) between nearest-neighbour spins.

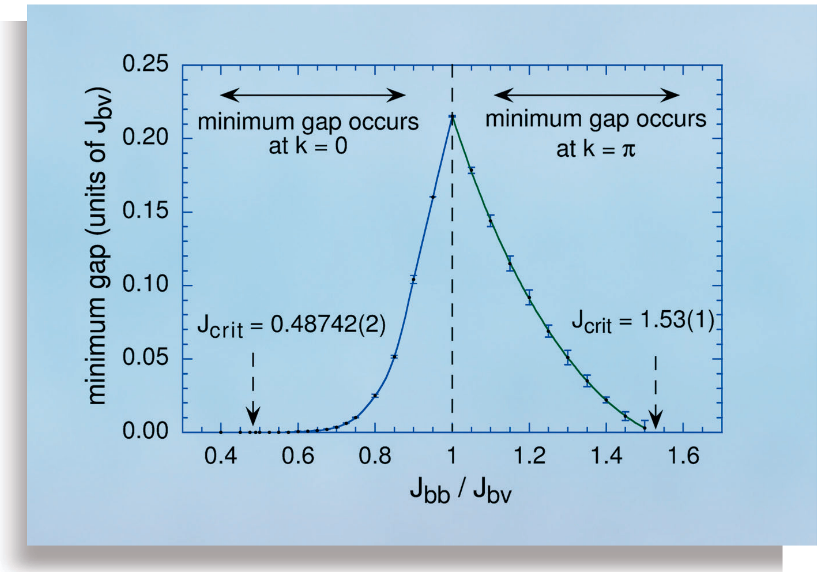

Figure 2: Gap to the lowest spin-one excited states of the sawtooth lattice vs. J_{bb}/J_{bv}, after extrapolation to infinite size.

Despite the large amount of theoretical work on these 1D spin systems, there is a lack of clear physical realizations of any of the various models discussed. However, experimental results that hold the promise of displaying quantum topological excitations have recently become available, involving overdoped delafossites $RCuO_{2+X}$ (where $R = Y$, La, etc.). The recent synthesis [1] of $YCuO_{2.5}$ has allowed one to elucidate its detailed structure, which suggests that the compound forms a nice realization of the Δ-chain, most likely with $J_{bb} < J_{bv}$.

Therefore, we analyze here the Δ-chain for various ratios J_{bb}/J_{bv} of these antiferromagnetic couplings. Now, for either $J_{bb} = 0$ or $J_{bv} = 0$ the system is equivalent to the Heisenberg chain. Thus, to understand the $YCuO_{2.5}$ compound, it is important to study the entire evolution of the elementary excitations from the sawtooth lattice to the Heisenberg chain as a function of J_{bb}/J_{bv}. The transition between these two limits is not immediately obvious: the symmetric Δ-chain has a small dispersionless gap with kink and antikink excitations, while the isotropic Heisenberg chain has no gap and pairs of so-called spinon excitations exhibiting a strongly dispersive spectrum.

We are unable to solve analytically and exactly for the wavefunction and dispersion for arbitrary J_{bb}/J_{bv}, but many of the important features of the spectrum can be obtained with high numerical precision by a careful exact diagonalization and extrapolation procedure. In this method, one extracts the eigenvalues and eigenvectors of the model spin Hamiltonian essentially exactly for finite-sized systems, in our case for up to 12 triangles (24 spin sites). This is possible because the Hamiltonian matrix, while large (roughly $2^{24} \times 2^{24}$), is also highly sparse (most elements are zero), and may be diagonalized by iterative approaches such as the Lanczos or Davidson methods. We then extrapolate the results to the infinite-size limit. Exact diagonalization, by now a well established technique, remains a flexible and powerful tool, capable of treating both ground and excited states with various momenta and spin quantum numbers and of extracting excitation gaps and dispersion spectra, and also of studying dynamical or thermodynamical properties.

Figure 2 summarizes the behavior of the excitation gap for the Δ-chain. We find [2] the lowest-lying excitations to have total spin quantum numbers $S_{tot} = 0$ and 1, which are degenerate within numerical error, thus giving a four-fold degeneracy overall. The gap is greatest when the spin couplings are equal ($J_{bb} = J_{bv}$), but decreases as J_{bb}/J_{bv} moves away from unity; at the same time, the spectrum, which is dispersionless for $J_{bb} = J_{bv}$, acquires increasing dispersion. The gap finally closes at wavevector $k = 0$ for $J_{bb}/J_{bv} < 1$ and at $k = \pi$ for $J_{bb}/J_{bv} > 1$. In this way, the gapped Δ-chain with equal couplings ($J_{bb} = J_{bv}$) goes over smoothly into the gapless Heisenberg chain ($J_{bb} = 0$ or $J_{bv} = 0$). By studying the wavefunctions, we find that the gap closure is related to the gradual disappearance of dimerization in the quantum ground state.

Preliminary low-temperature susceptibility measurements on $YCuO_{2.5}$ suggest a gap with J_{bv} of order 80 K or more, a reasonable value for this system. Further experiments and detailed comparison with our numerical results will permit one to determine whether the Δ-chain model is applicable to this compound, and if so to infer the value of J_{bb}/J_{bv}. This first complete theoretical study should assist the interpretation of these interesting experiments. ▮

---

[1] G. Van Tendeloo, O. Garlea, C. Darie, C. Bougerol-Chaillot, and P. Bordet, J. Solid State Chem. **156,** 428 (2001).

[2] S. A. Blundell and M. D. Núñez-Regueiro, Eur. Phys. J. B **31** (Rapid Note), 453 (2003);
J. Phys. Condens. Matter **16,** S791(2004).

Contact: sblundell@cea.fr

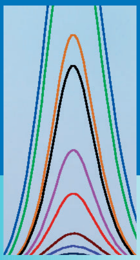

OSCILLATIONS OF THE LONGITUDINAL MAGNETO-RESISTANCE IN 2D METALLIC SYSTEMS

T. Champel and V. P. Mineev

Service de Physique Statistique,
Magnétisme et Supraconductivité
(SPSMS), DRFMC

The quantum theory of magneto-resistance for currents perpendicular to the layers in quasi two-dimensional metals is developed. It is found that a pseudo-gap structure in the spectral conductivity between the Landau levels is responsible for the inverse thermal activated dependence of the resistivity maxima experimentally observed in high magnetic fields.

Nous développons la théorie quantique de la magnéto-résistance pour des courants perpendiculaires aux couches de métaux quasi bi-dimensionnels. Nous trouvons qu'une structure avec un pseudo-gap dans la conductivité spectrale entre les niveaux de Landau explique la variation expérimentalement observée des maxima de résistivité en champ magnétique élevé. Ces derniers suivent une loi d'activation thermique inversée.

The electronic properties of metals are essentially described in terms of a gas of electrons. The electronic states are then characterized by the electron momentum k and the energy ε which is a continuous function of the momentum: $\varepsilon = h^2 k^2/2m$ where m is the electron mass. Each state with a given k can be occupied twice only (spin up and spin down states), which leads at zero temperature to filling of all the states with energies ε below some energy ε_F (the so-called Fermi energy).

If we apply a magnetic field *H* to a metal, the continuous set of electronic states transforms to discrete levels, called Landau levels, which have quantized values for the energy $\varepsilon = h\omega_c(n+1/2) + h^2 k_z^2/2m$, where *n* is an integer, $\omega_c = eH/mc$ the cyclotron pulsation and k_z the momentum along the field direction z. These levels are strongly degenerated and the degeneracy is proportional to the magnetic field. Let us neglect for a moment the dispersion along z. Then again, at zero temperature, all fully occupied Landau levels lie below the Fermi energy. With increasing magnetic field, both the energy and the degeneracy of the Landau levels increase. Hence when the highest filled Landau level intersects the Fermi level the electrons are transferred to lower states. For a higher value of magnetic field the process is repeated with the next Landau level, and so on. On the macroscopic scale, this periodic process manifests itself through oscillations of the magnetization (the “de Haas-van Alphen” effect) or the resistance (the “Shubnikov-de Haas” effect) with the magnetic field.

Actually, if one considers k_z, the Fermi energy is crossed by many occupied Landau levels. The non-quantized states available for any amplitude of magnetic field act as a reservoir. The discrete nature of the Landau levels is thus blurred. As a result, the oscillations of the magnetization or of the magneto-resistance become relatively small.

The quantitative theory of the magnetic quantum oscillations in 3D-metals was proposed in 1955 by Lifshitz and Kosevich. It has been verified by many experiments and is still used to determine the real Fermi surface of metals.

Recently, there has been a renewed interest in the study of compounds with strongly anisotropic electronic properties in high magnetic fields. For example, in layered heterostructures, a 2D-electron gas can be artificially achieved. In this case, there is no Landau level broadening due to dimensionality ($k_z=0$), and the oscillations of the thermodynamic and transport properties can therefore be very strong. Also, compounds such as synthetic metals based on organic salts are naturally low-dimensional electronic systems: they can usually be described in terms of a quasi 2D gas of electrons, i.e. they consist of highly conducting planes with a small electron hopping probability between the layers.

Features of the magnetic quantum oscillations are known to be noticeably different in 2D systems compared to 3D systems. For example, the 2D de Haas-van Alphen effect is characterized by a sharp sawtooth-like shape at low temperatures,

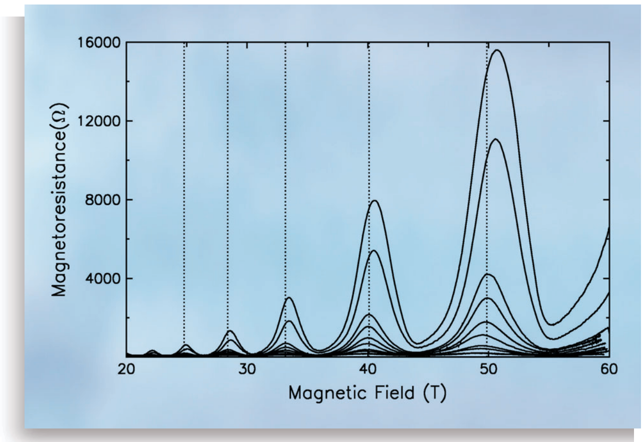

Figure 1 : Oscillations of ρ_{zz} in the layered conductor β''-(BEDT-TTF)$_2$SF$_5$CH$_2$CF$_2$SO$_3$ measured at different temperatures (from the top, 0.59, 0.94, 1.48, 1.58, 1.91, 2.18, 2.68, 3.03, 3.38, 3.80, and 4.00 K) (data from [2]).

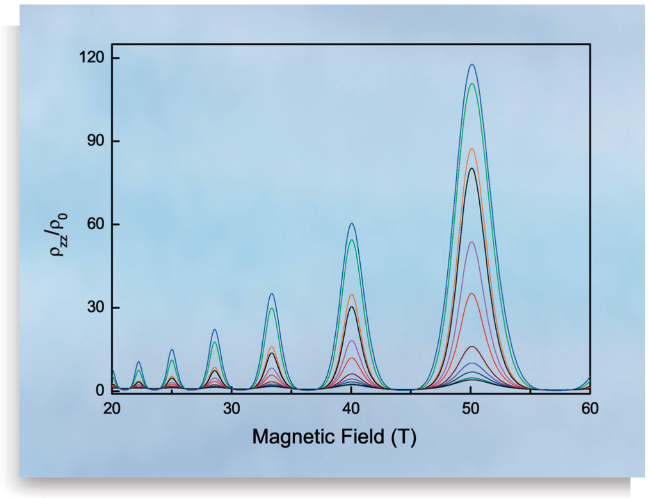

Figure 2 : Theoretical oscillations of ρ_{zz}/r_0. The different curves correspond to the same temperatures as shown in Fig. 1; ρ_0 is the resistance at zero magnetic field and zero temperature.

while the oscillations of the magnetization in 3D metals are always smooth.

In quasi 2D systems, the situation concerning the Landau level broadening is in some sense intermediate between the 2D and 3D cases and depends on the distance $h\omega_c$ between these levels compared to the interlayer coupling energy: the Landau level broadening due to dimensionality is large at relatively small magnetic fields. At very high magnetic fields, broadening only occurs through impurity effects, exactly like in 2D systems. The (semi-phenomenological) theory of the de Haas-van Alphen effect in quasi 2D systems has revealed a crossover between the 2D and 3D limits for the behaviour of the magnetization oscillations.

It is with the same idea of an apparent dimensionality reduced by the magnetic field that we studied the magneto-resistance oscillations in quasi 2D systems [1]. We were rather interested in the limit of high magnetic fields, motivated by the experiment of Nam *et al*. [2] on the organic layered conductor β''-(BEDT-TTF)$_2$SF$_5$CH$_2$CF$_2$SO$_3$. Giant Shubnikov-de Haas oscillations of the longitudinal magneto-resistance ρ_{zz} have been observed at high magnetic fields and low temperatures (see Fig. 1 taken from [2]; here *z* is the direction of the magnetic field which is perpendicular to the layers). In particular, a regime with an inverse thermally activated behaviour of the maxima of the magneto-resitivity ρ_{zz} has been pointed out for magnetic fields higher than 20 T [2]. Such a feature is completely absent in the 3D Shubnikov-de Haas theory.

Our analytical calculations [1], developed in the framework of the quantum transport theory, have revealed a pseudo-gap structure in the spectral magneto-conductivity $\sigma_{zz}(\varepsilon)$ between the Landau levels in high magnetic fields. In other words, when the energy of the electrons lies between the Landau levels, the conduction at a finite low temperature *T* is determined by the thermal excitation at the edges of the gap-like interval Δ between the levels. This explains why the maxima of ρ_{zz} have an inverse thermally activated temperature dependence: $\rho_{zz}^{max} \sim \exp(\Delta/T)$. At very low temperatures, quasi-particles whose energy lies in the pseudo-gap range Δ mainly contribute to conduction, then the resistivity maxima saturate.

Our numerical calculations of ρ_{zz} at different finite temperatures shown in Fig. 2 reproduce well the appearance of huge oscillations under the same conditions of temperatures and magnetic fields as in experiment [2]. In particular we successfully obtain inverse thermal activation of ρ_{zz} maxima for fields $H \geq 20$ T.

---

[1] T. Champel and V. P. Mineev, Phys. Rev. B **66,** 195111 (2002).
[2] M. S. Nam et al., Phys. Rev. Lett. **87,** 117001 (2001).

Contact: vmineev@cea.fr

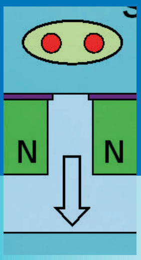

Spatial structure of Cooper electronic pairs from current noise measurements

M. Houzet

Service de Physique Statistique,
Magnétisme et Supraconductivité
(SPSMS), DRFMC

Measuring the fluctuations of electrical current has recently proved a way to obtain new information on mesoscopic devices. In a superconductor attached to two normal metallic leads, the cross-correlation of the currents flowing in each of them is shown to provide information on the spatial structure of the Cooper pairs.

Il a été récemment prouvé que la mesure des fluctuations du courant électrique permet d'obtenir de nouvelles informations sur des dispositifs mésoscopiques. Nous montrons que, pour un supra-conducteur relié à deux électrodes métalliques normales, la corrélation croisée des courants circulant dans chaque électrode fournit des informations sur la structure spatiale des paires de Cooper.

◆

Tunnel junctions are formed with two pieces of normal metal separated by a thin oxide layer. They are named after the quantum tunnelling of single electrons which allows electrical current to flow through the insulating barrier. When one of the electrodes becomes superconducting, the conduction electrons attract each other into Cooper pairs. A gap in the energy spectrum hinders single electron excitations. As a result, the standard tunnelling of single electrons is barred. Instead, Andreev reflection - a process involving two electrons - is observed. It allows a Cooper pair from the superconductor to be transferred into two electrons on the other side of the junction. Equivalently, it can be viewed as the reflection of an incident quasi-hole from the normal electrode into a quasi-particle in the same electrode. This process is expected to take place on a characteristic distance of about the size of the Cooper pairs.

In principle, it should be possible for the electrons to be transmitted in two different normal terminals provided that the distance between the contacts is comparable with the size of the pairs. This process, called the crossed Andreev reflection (CAR), could be useful to probe the spatial structure of the Cooper pair directly, but how can it be detected? It was first suggested to perform conductance measurements on multi-terminal devices like the one represented in Fig. 1. Indeed, applying a voltage to lead B would affect the current flowing between the superconductor and lead A if the normal leads were close enough. However this procedure has two main drawbacks. First, CAR comes along with elastic co-tunnelling (EC), the transfer of an electron from one normal lead to the other one, via the superconductor, see Fig. 2. Second, CAR and EC contributions to the average currents are dominated by direct Andreev reflection in each normal lead, i.e. by the current associated

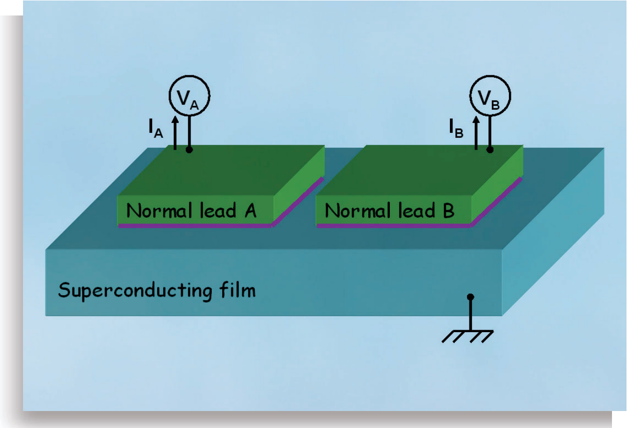

Figure 1: Schematic representation of the three-terminal device.

with the transfer of a Cooper pair of the superconductor into two electrons in the same lead. Alternatively, we found that the CAR or the EC contribution can be picked up directly by measuring the cross-correlation of the currents flowing in each normal lead [1].

As a matter of fact, due to the discrete nature of the electric charges, current fluctuates in time around its mean value. It is characterised by the current noise, $S_{\alpha\beta}=2\int dt\,\delta I_\alpha(t)\delta I_\beta(0)$, where $\delta I_\alpha(t)=I_\alpha(t)-I_\alpha$ describes the fluctuations of the instantaneous current, $I_\alpha(t)$, around its mean value, I_α, and α, β stand for any normal lead A,B. Current noise measurement revealed a powerful probe for electronic devices. In two-terminal junctions, the equilibrium noise is simply proportional to the temperature T and the conductance G of the junction, $S=4k_BTG$, according to the fluctuation-dissipation theorem. By contrast, at vanishing temperature, the non-equilibrium noise is proportional to the current and the absolute electric charge q, transferred through the junction. In the case of rare and uncorrelated charge transfers, like in quantum tunnelling, $S=2qI$ was predicted. As a result of the Andreev reflection, which involves two electrons, this noise is doubled in a hybrid superconducting/normal metallic tunnel junction ($q=2|e|$) compared to a completely normal device ($q=|e|$). Such doubling of the noise was first observed in our laboratory [2].

The cross-correlation, S_{AB}, in the three-terminal hybrid structure represented in Fig. 1 also deserved some attention. Indeed, it was predicted not only to differ by a numerical factor, but also to show a sign change with respect to normal metallic structures [3]. A simplified explanation of this effect is the following. If electrons in the two leads are emitted from one Cooper pair, a positive correlation is expected, since both electrons appear at the same time in each lead. By contrast, in the normal structure, electrons arriving one by one at the barriers are transmitted either in one or the other lead, leading to a negative correlation.

We find that CAR contributes to the cross-correlation with a positive sign, while EC contributes with a negative sign, and there is no contribution at all from direct Andreev reflection. The CAR and EC contributions can be selected independently by tuning the voltages of the normal terminals. In particular, only CAR contributes when the voltages are the same in each normal electrode, while only EC contributes when the voltages are opposite. Cross-correlation in tunnelling systems thus provides a direct way (i) to probe both CAR and EC and (ii) to measure the sign change of the correlations.

Our quantitative estimates of these effects show that their observation may be within the reach of present technology. The characteristic size for the Cooper pairs gives the important scale to be achieved in the real device: a few tens of nanometres for standard materials. Then the overall amplitude of the signal to be measured would compare with the resolution already achieved in the experiment [2]. The main difficulty of the experiment is to make the contacts as close as possible, without short-circuiting them. We hope that the experiment can be performed soon in our laboratory to compare with our predictions.

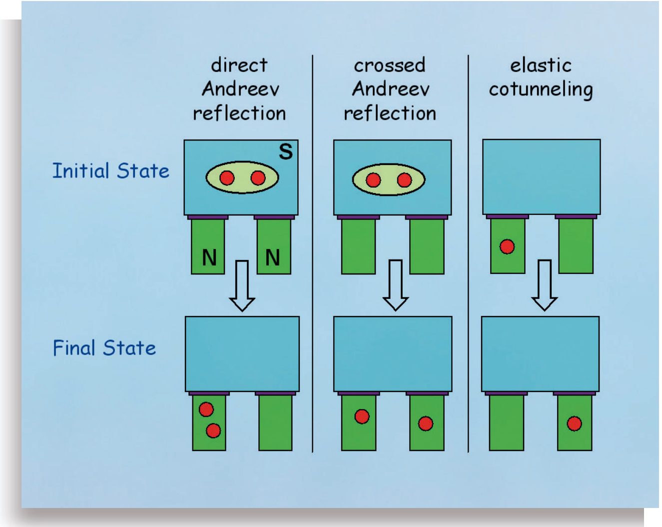

Figure 2: Three processes for charge transfer.

---

[1] G. Bignon, M. Houzet, F. Pistolesi, and F. W. H. Hekking, Europhys. Lett. **67,** 110 (2004).
[2] F. Lefloch, C. Hoffmann, M. Sanquer, and D. Quirion, Phys. Rev. Lett. **90,** 067002 (2003).
[3] J. Torrès and T. Martin, Eur. Phys. J. B **12,** 319 (2001).

Contact: mhouzet@cea.fr

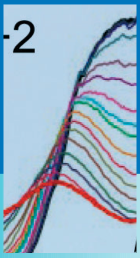

THE KONDO EFFECT: FROM MACRO TO NANOSCALE

M. Lavagna[a], **P. Vitushinsky**[a], **and A. Jerez**[b]

a: Service de Physique Statistique, Magnétisme et Supraconductivité (SPSMS), DRFMC
b: European Synchrotron Radiation Facility, Grenoble

The Kondo effect is responsible for an anomalous low temperature behavior of resistivity in certain metallic alloys. Recently fabricated quantum dots (QD) have led to a spectacular revival of this effect. We discuss here interferometry experiments with QD allowing for a direct measurement of the transmission phase shift, a fundamental quantity of the Kondo effect.

L'effet Kondo est responsable du comportement anormal de la résistivité à basses températures dans certains alliages métalliques. L'élaboration récente de points quantiques (QD) a conduit à un renouveau spectaculaire de cet effet. Nous discutons ici des expériences d'interférométrie en présence de QD permettant d'accéder au déphasage de transmission, une quantité fondamentale de l'effet Kondo.

●

I. THE KONDO EFFECT IN BULK SYSTEMS

The electrical resistivity of metals monotonously decreases when the temperature is lowered. Yet it was discovered in the early 60's that the resistivity of metals containing magnetic impurities exhibits a logarithmic increase as the temperature is lowered. This is the Kondo effect which takes place when an antiferromagnetic spin interaction exists between a localized magnetic impurity and the conduction electrons. This effect results from a spin-flip of the impurity after each collision with a conduction electron. The so-called Kondo temperature, T_K, emerges characterizing a crossover between the high temperature regime ($T>T_K$) where the impurity spin is almost free, and the low temperature regime ($T<T_K$) where one conduction electron constitutes a singlet state with the impurity spin. The enhanced resistivity observed at low temperature results from the increased scattering cross-section of the conduction electrons off this singlet. During the scattering process, the phase of the conduction electron wave function is changed. This phase shift, δ, was predicted more than three decades ago to be $\pi/2$. A measurement of this phase shift, out of scope in bulk metals, has now been made possible in QD.

II. THE KONDO EFFECT IN QUANTUM DOTS

QD can be obtained in a controlled fashion thanks to recent progress in nanolithography [1]. The QD are coupled to two metal leads by tunnel barriers. By acting on the gate voltage V_G, the number N of electrons confined in the dot can be changed. Due to its small size, the electronic energy spectrum in the dot is discrete and V_G permits tuning of the energy levels. This is the Coulomb blockade phenomenon where periodic conductance peaks as a function of V_G are separated by almost zero conductance valleys (Fig. 1a). Two different regimes occur depending on the parity of N. If N is even (odd), the conductance decreases (increases) when the temperature is lowered [2]. This asymmetry between the behaviour observed in conductance valleys of different parity, is a signature of the Kondo effect that takes place in odd valleys. Indeed, when an odd number of electrons is trapped within the dot and when the energy of the topmost singly-occupied level in the dot is far below the Fermi energy of the leads, a virtual process takes place (Fig. 1b) leading to a spin-flip in the QD. This is precisely the Kondo effect presented above, where the impurity is substituted by the QD. Note that in QD, the Kondo effect results in an enhancement of the conductance and not of the resistance as in bulk metals.

III. TRANSMISSION PHASE SHIFTS

An Aharonov-Bohm interferometer is a device made of two conducting arms, threaded by a magnetic flux. It enables the quantum interference between the wave functions of electrons passing in each of the arms to be observed. By embedding a QD in one arm (see inset in Fig. 2), the phase shift δ experienced by the electron wave-function as it passes through the QD can be measured. The evolution of δ as a function of V_G has been obtained in recent experiments [3] (Fig. 2). The results are surprising: a smooth increase of δ with V_G is observed, with a value in the Kondo regime close to π which differs from earlier theoretical predictions.

In order to clarify the experimental situation, we have theoretically taken into account the difference of geometry between a QD and the bulk metal. The transmission phase shift introduced by the QD is analyzed in terms of a scattering problem in one dimension instead of three dimensions in bulk metals. We have shown that this leads to a drastic change in the phase shift [4]. Using Landauer's formula, we established the relation $G \propto \sin^2(\delta/2)$. Figure 2 compares this theoretical prediction with experimental data and, as can be seen, the agreement found is very good. Moreover we have shown that the phase shift is related to the average number of particles in the localized level n_d according to a generalized Friedel sum rule. By performing exact Bethe-Ansatz calculations in the Anderson model, we can determine n_d , and hence δ. In the presence of a single fitting parameter corresponding to the coupling strength between the dot and the metal leads, the agreement between theoretical and experimental results are very satisfactory.

Our project is to now extend our analysis to the presence of a magnetic field and to other situations leading to the existence of new regimes characterized by non-Fermi liquid behaviour reminiscent of the multichannel Kondo effect [5].

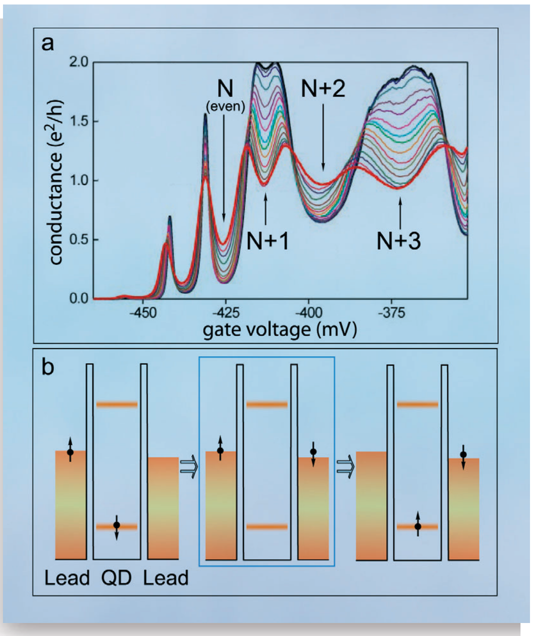

Figure 1: (a): Experimental conductance of a QD as a function of the gate voltage V_G which changes the number of electrons, N, confined in the QD. Depending on the parity of N, the conductance decreases or increases when the temperature is lowered from 1K (red) to 25mK (black) (from [2]). (b): Schematization of one of the virtual tunnelling processes in the QD-lead device leading to a spin-flip in the QD.

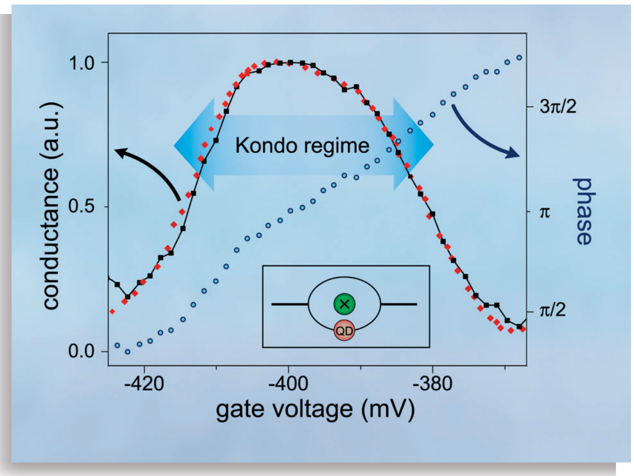

Figure 2: Comparison of the theoretical (black curve) and experimental (red points) conductances. The experimental values (from [3]) for G and δ as a function of V_G, are reported as red and blue points, respectively.

Acknowledgements

We thank D. Bensimon for collaboration on related subjects and L. Saminadayar, C. Baüerlé, P. Simon, D. Feinberg and F. Hekking with whom we are carrying out a common project on this topic within the "Institut de Physique de la Matière Condensée" of Grenoble.

[1] L. Kouwenhoven and L. Glazman, Physics World **14,** 33 (2001).
[2] W.G. van der Wiel et al., Science **289,** 2105 (2000).
[3] Y. Ji, M. Heiblum, and H. Shtrikman, Phys. Rev. Lett. **88,** 076601 (2002).
[4] P. Vitushinsky, A. Jerez and M. Lavagna, Proceedings of the Vth Rencontres de Moriond en Physique Mésoscopique, edited by C. Glattli, M. Sanquer, and J. Trân Thanh Vân (Editions EDP Sciences, Les Ulis/France, 2004).
[5] A. Jerez, M. Lavagna, and D. Bensimon, Phys. Rev. B **68,** 094410 (2003); M. Lavagna, A. Jerez, and D. Bensimon in *Concepts in Electron Correlation* Vol 110, edited by A.C. Hewson et V. Zlatic (Kluwer Academic Press, Amsterdam/The Netherlands, 2003) p. 219

Contact: mlavagna@cea.fr

Charge transport in DNA

S. Roche

Service de Physique Statistique,
Magnétisme et Supraconductivité
(SPSMS), DRFMC

Charge transport in deoxyribonucleic acid (DNA) is investigated in view of its biological implication in damage and repair, protein bonding, and integration in (bio)electronics or DNA-based chips. We discuss basics of charge transport in the quantum coherent regime, and show that some concepts of electronic conduction need to be revisited for DNA.

Le transport de charge dans l'acide désoxyribonucléique (ADN) est étudié du fait de son implication dans les lésions et la réparation, les liaisons des protéines, et l'intégration dans des composants (bio)électroniques ou basés sur l'ADN. Nous discutons les fondements du transport de charge en régime cohérent quantique et nous montrons que certains concepts de conduction électronique doivent être réexaminés.

The double-helix structure of DNA is made from two weakly hydrogen-bonded strands, each of which consists of a sequence of four nucleotides (A-adenine, T-thymine, C-cytosine, G-guanine). Pairing of the bases belonging to two strands strictly follows the Watson-Crick complementarity law (i.e. interstrand pairs only appear as AT or CG). Due to the smaller ionization potential of the guanine, charge transport is believed to be conveyed through the highest occupied molecular orbitals of this base (HOMO-G).

In recent years, two kinds of experiments have provided valuable information on charge transfer in DNA. First, fluorescence experiments have relied on the use of intercalated metallic complexes acting as donor and acceptor to photo-induce and follow charge migration along small DNA fragments [1]. Such experiments have pointed towards an efficient transfer over unprecedented length scale for biomolecules. Other experiments have focused on contacting DNA with conducting electrodes, and performing mesoscopic conductance measurements under various physical conditions. Presently available results lack consistency since all kinds of transport regimes have been proposed, from metallic-like, superconducting, semi-conducting to strongly insulating behaviors. Transport mechanism might be purely hole- or polaron-based.

We have recently performed a theoretical study on several kinds of both artificial or genomic DNA. To discuss basic transport mechanisms, we have elaborated on a modelling of hole transport through the guanine bases, described within an effective 1D tight binding Hamiltonian [2],

$$H = \sum - t_{\mathrm{DNA}} \cos(\theta_{n,n+1})(c_n^{\dagger} c_{n+1} + h.c.) + \varepsilon_n c_n^{\dagger} c_n$$

$c_n^{\dagger}$ (c_n) is the operator corresponding to charge creation (annihilation) at site n, t_{DNA} gives the amplitude of π-π coupling between nearest neighbour orbitals, ε_n the hole site energies and cos ($\theta_{n,n+1}$) is temperature-dependent and describes the lowering of coupling between base pairs due to thermal fluctuations [3].

Landauer formalism

In the Landauer formalism used here, one considers an electronic wavepacket of amplitude unity, wave vector k and energy E which is injected from a metallic contact (see figure) inside a DNA sequence. The coefficients R and T give the amplitudes which are respectively reflected by the DNA sequence and transmitted to the other metallic contact. Current conservation implies $R + T = 1$. The inverse transmission rate R/T is related to the dimensionless resistance ρ, and for weak transmission, the DNA resistivity is proportional to $[(1-T_{av})/T_{av}]\ S_{DNA}/L_{DNA}$ taking T_{av} an average of the transmission coefficient for energies close to the HOMO-G ionisation energy, $S_{DNA}=3.10^{-18}m^2$ the average DNA cross section, and L_{DNA} the sequence length [3].

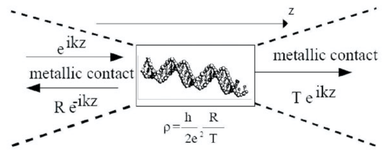

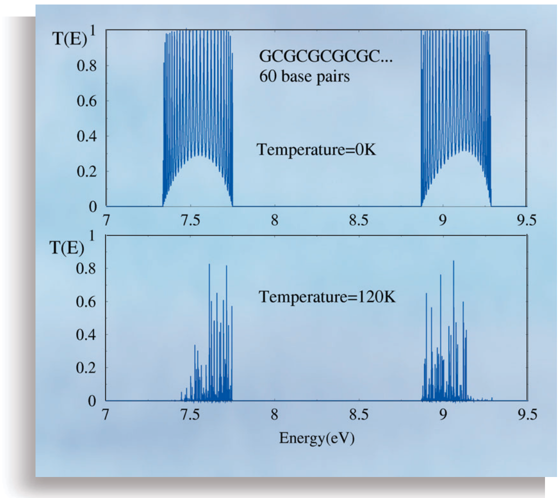

Figure 1: Theoretical transmission coefficients for periodic Poly(dG)-Poly(dC) sequences with 60 base pairs, at two temperatures.

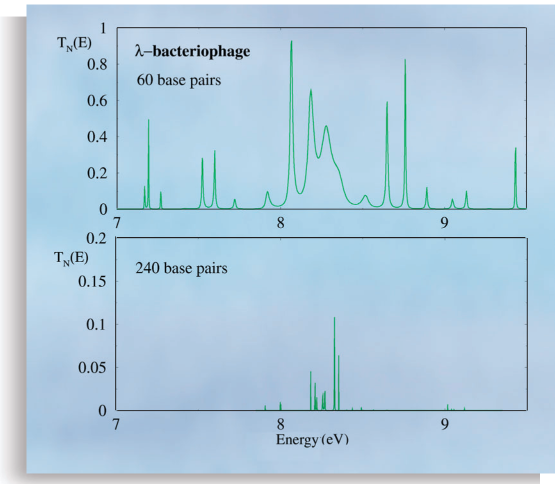

Figure 2: Theoretical transmission coefficients for λ-bacteriophage-based sequences with increasing number of base pairs.

In order to evaluate the conductivity of the system, we use the Landauer formulation of electron transmission (see inset) and compute the energy-dependent transmission coefficient *T(E)*. Our modelling is such that the full energy dependence of *T* is necessary to discuss the charge transfer properties, although the DNA chain is connected to metallic leads and the electrode Fermi levels are lined up to the HOMO-G.

We have considered synthetic Poly(dG)-Poly(dC) sequences consisting of G and C bases alternated on each strand and sequences extracted from the biological λ-bacteriophage or from the Human Chromosome 22 DNA. The transmission coefficient was studied for finite sequences from 20 nm up to 200 nm long, i.e. representing 60 to 600 pairs of bases.

As expected, Poly(dG)-Poly(dC) sequences were found to follow a “semi-conducting-like” regime mainly due to a transmission gap stemming from the two spectral bands (see Fig. 1). Temperature was found to reduce coherent charge transfer, but theoretical calculation for the DNA resistivity was in good agreement with some experimental estimates.

Differently, λ-bacteriophage or Chromosome 22-based sequences were found to exhibit much more resistance to charge transport [3]. Actually, each specific {A,T,C,G}-based sequence follows a complex order which lacks periodicity, although encompassing long range correlations. In our modelling of hole transport through the HOMO-G, any other A, T or C nucleotide acts as a potential barrier that reduces coherent tunnelling, so that larger aperiodic chains exhibit strong backscattering efficiency irrespective of the energy of the injected charges [3]. This phenomenon is illustrated in Fig. 2 for λ-bacteriophage-based sequences with increasing number of base pairs.

The nature and contribution to charge transfer of long range correlations that display complex patterns in different genomic chains have also been the subject of a full study. It was shown that if compared with random sequences with uncorrelated distribution of nucleotides, charge transfer in Chromosome 22-based sequences was found to be much more efficient [4].

In the genomic sequences, it is not possible to estimate any resistivity since resistance increases considerably with sequence length. Thermal fluctuations that reduce π–π coupling strength between intrastrand next neighbour nucleotides also strongly disfavour charge transport. From our calculations, it appears that strong insulating behaviours are expected for length above ∼ 10 nm in genomic sequences, and that periodic synthetic sequences may sustain long range transport over 20 nm at small temperatures.

To summarize, we have presented some charge transport modelling and basic results concerning artificial and biological DNA. The charge transfer was shown to be critically dependent on the sequence nature and length of base pairs as well as thermal fluctuations.

[1] C. R. Treadway, M. G. Hill and J. K. Barton, Chem. Phys. **281,** 409 (2002).
[2] M. A. Ratner, Nature (London) **397,** 480 (1999).
[3] S. Roche, Phys. Rev. Lett. **91,** 108101 (2003).
[4] S. Roche, D. J. Bicout, E. Macià, and E. I. Kats, Phys. Rev. Lett. **91,** 228101 (2003).

Contact: sroche@cea.fr

EPITAXY, SURFACE INSTABILITIES AND ROUGHNESS

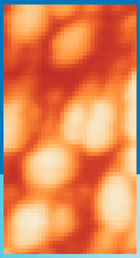

J. Villain

Service de Physique Statistique,
Magnétisme et Supraconductivité
(SPSMS), DRFMC

Instabilities during epitaxial film growth may either be modelled by a linear equation, or follow a slow thermal activation process. It is shown here that a third model is possible in a growing crystal, when roughness is first induced by growth and generates bumps that eventually reach a critical size.

Dans un film épitaxié, les instabilités lors de la croissance peuvent être modélisées par une équation linéaire ou suivre un processus lent d'activation thermique. Nous montrons qu'un troisième modèle est possible lorsque la rugosité est d'abord induite par la croissance et qu'elle génère des îlots qui atteignent une taille critique.

In semiconductor technology, epitaxial crystal films are often grown in the (001) direction. Their surface is initially smooth, but bumps often appear during growth. These bumps can then be "buried" and used as quantum dots. A picture of such quantum dots of GaN on AlN, obtained by atomic force microscopy, is shown in Fig. 1.

These bumps originate from an instability of the smooth surface, which results from the misfit between the crystal constants of the substrate (a_0) and of the film ($a = a_0 + \delta a$). If the surface is flat, the epitaxial film must accept the crystal constant of the substrate. In contrast, if bumps are present, this constraint is partly relaxed at the top of a bump. Thus, a surface with bumps has a lower energy than a flat surface, which is therefore unstable. In the simplest cases, the height $h(t)$ of the bump (Fig. 2) evolves with time t according to the linear differential equation

$$\frac{d}{dt}h = Kh \qquad (1)$$

and the smooth surface is unstable if $K>0$. In the case of a crystal surface, formula (1) can be derived assuming [1,2]: (i) no dislocations (especially no misfit dislocations), (ii) a temperature higher than the so-called "roughening transition temperature" T_R of the surface, above which the surface becomes rough as an effect of thermal fluctuations. Condition (i) is verified, at least below a critical thickness, for films of Ge on Si, for InAs/GaAs, etc. Condition (ii) is probably not verified for the (001) surface of semiconductors. Also, in practice, h in Eq. (1) is the amplitude of a sinusoidal surface height modulation of wavelength R. Because K depends on h and R, Eq. (1) is actually a non-linear equation. In the remainder of this article, condition (ii) is assumed not to be verified. We therefore consider that film growing is at the origin of instabilities rather than thermal fluctuations.

The energy of a bump consists of two terms: a capillary surface energy δF_{cap} which tends to reduce the bump area, and an elastic energy δF_{el} which favours its creation in order to reduce the stress in the film. A calculation based on standard elasticity yields for a bump of volume R^2h (with $h<R$)

$$\delta F_{el} \approx -M\varepsilon_0^2 R h^2 \qquad (2)$$

where M is a combination of elastic constants and $\varepsilon_0 = \delta a/a$ is the misfit between the lattice constants of the substrate and the adsorbate. For $T<T_R$, the surface free energy is

$$\delta F_{cap} \approx \gamma_s R h \qquad (3)$$

where γ_s is the free energy of a unit length

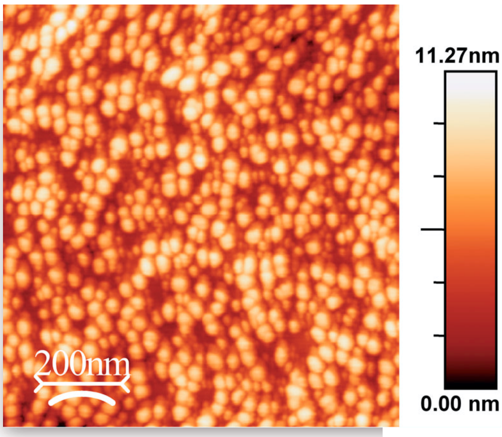

Figure 1: Atomic force microscopy of quantum dots of GaN grown on a AlN substrate. The colour scale indicates the depth profile (courtesy of B. Daudin).

step. A step is the edge of a new atomic layer. γ_s would vanish for $T>T_R$. The smooth surface is unstable with respect to bump formation if $\delta F_{cap} + \delta F_{el} < 0$. This implies $h > h_c$ with

$$h_c = \frac{\gamma_s}{M\varepsilon_0^2} \qquad (4)$$

Thus, the instability appears only after the bump has reached a sufficient size. Below that size, the energy is positive. There is an activation energy $\Delta F \approx M\varepsilon_0^2 R h_c^2$.

It may be shown that R should be of the order of h_c so that $\Delta F \approx M\varepsilon_0^2 h_c^3 \approx \gamma_s^3 M^{-2} \varepsilon_0^{-4}$. To summarize, there is an "activated" instability for $T<T_R$, while for $T>T_R$ the instability is "linear", i.e. described by the linear equation (1). But this is not the whole story. A third type of instability is possible, as will be seen now [4].

In the above argument indeed, growth has been ignored. The remainder of this report is devoted to the case of a growing crystal surface below T_R. The problem is the following. At the temperatures used in epitaxial growth, the (001) surface of a semiconductor has very few steps at thermal equilibrium. However when the film grows, it necessarily has a non-vanishing density of steps which depends on the growth rate. Tersoff [3] has suggested that a crystal surface which is smooth at equilibrium (i.e. $T<T_R$) becomes rough when it grows. Tersoff introduced elasticity into a work by Nozières & Gallet which is a part of the Holy Writ of crystal growth. In both papers, roughness is postulated rather than demonstrated. Tersoff's conclusion is that the instability of a growing epitaxial film is described by a linear equation. This can be correct in certain cases, but in many problems the effect of time (ignored by Tersoff) should be carefully taken into account [4].

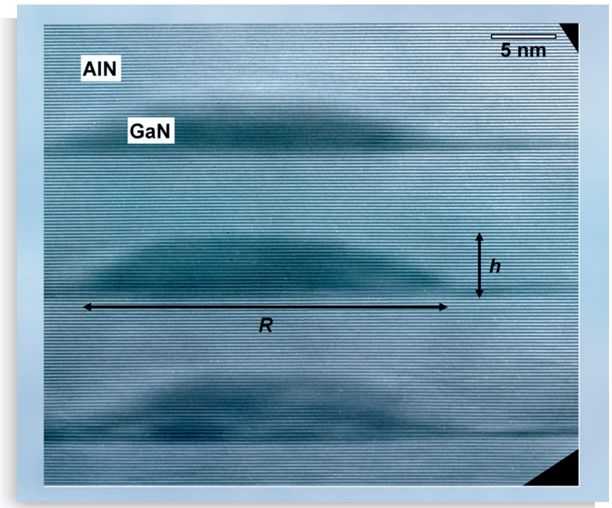

Figure 2: Transmission electron microscopy of a cut of GaN quantum dots (dark grey) in a matrix of AlN (light grey). The lateral dimension R and the height h of a dot are indicated (courtesy of J.-L. Rouvière).

As said above, the usual situation in semiconductor technology is that of an initially smooth (001) surface. Even in the absence of any misfit, growth generates a roughness of the surface as a result of random nucleation of new atomic layers. It increases with time. At infinite time, a growing surface is (kinematically) rough, in agreement with the statements of Nozières & Gallet, and Tersoff. However, for an infinite surface, a steady regime is not reached in any finite time! The maximum lateral size $\zeta(t)$ of the bumps and holes generated by random nucleation goes to infinity with time, as does their maximum height $h_1(t)$. Scaling arguments suggest $h_1(t) \propto \zeta^{\alpha}$ with $\alpha > 0$.

A weak misfit is not expected to change this situation for short times. After some time, however, the size of the bumps created by random nucleation becomes larger than the size h_c given by (4). Then an instability should take place, driven by elasticity and misfit rather than nucleation randomness. At long enough times, the evolution may follow the linear equation (1) which triggers an exponential increase, $h(t) \propto \exp(Kt)$. However, this period is preceded by a long one where the instability does not show up. The instability sets in at a fairly well-defined time, in contrast with both linear and activated instabilities. It is a new type of instability [4]. The above description is in qualitative agreement with experiment for weak misfits ($\delta a/a<2\%$). The case of large misfits (which is of greater practical interest) is different. Nucleation occurs suddenly at a critical coverage. We are currently developing a model which takes into account the distortion at the edges of a new atomic layer, which probably drives the formation of the bump.

[1] A. Pimpinelli, J. Villain, *Physics of Crystal Growth* (Cambridge University Press, Cambridge/U.K., 1998) and references therein.
[2] P. Politi, G. Grenet, A. Marty, A. Ponchet, and J. Villain, Physics Reports **324**, 271 (2000) and references therein.
[3] J. Tersoff, Phys. Rev. Lett. **87,** 156101 (2001).
[4] J. Villain, C.R. Physique **4,** 201 (2003) and references therein.

Contact: jvillain@cea.fr

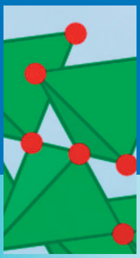

ENHANCED MAGNETO-CALORIC EFFECT IN FRUSTRATED MAGNETS

M. E. Zhitomirsky

Service de Physique Statistique, Magnétisme et Supraconductivité (SPSMS), DRFMC

The magneto-caloric effect is characterized by a temperature change in response to a variation of an applied magnetic field; this effect is especially important in frustrated magnets. The thermodynamics of demagnetization of such systems, from a fully polarized state at high field to a partially polarized one at low field, are theoretically discussed.

L'effet magnéto-calorique se caractérise par une variation de température en réponse à une variation du champ magnétique appliqué; cet effet est particulièrement important dans les systèmes magnétiques frustrés. La thermodynamique de la désaimantation de tels systèmes, entre un état totalement polarisé à fort champ et un état partiellement polarisé à faible champ, est théoriquement discutée.

The term frustration generally describes a competition between various forces and interactions without a definite win. Such a competition leads to a large residual degeneracy of low-energy states. It is for instance responsible for unique properties of water ice, superconducting Josephson junction arrays, neural networks, and new magnetic materials [1]. Geometrical frustration develops in magnetic insulators with special types of crystal lattices (see inset 1). Kagomé and pyrochlore lattices shown in Fig. 1 are two examples achieved, for instance, in $SrCr_{9p}Ga_{12-9p}O_{19}$ and in $Gd_2Ti_2O_7$ respectively. Antiferromagnetic exchange interaction between local spins S on such lattices is unable to stabilize a unique spin configuration. It is always possible to rotate finite groups of spins without any energy cost. At low temperatures the system fluctuates between an infinite number of isoenergetic spin configurations. No conventional magnetic ordering is possible at low temperatures in such frustrated magnets [2].

Macroscopic degeneracy of frustrated antiferromagnets persists in external magnetic fields up to a so-called saturation field H_{sat} [3]. This field is of the order of the exchange constant J and depends on the lattice: $H_{sat}=6JS$ for Kagomé and $H_{sat}=8JS$ for pyrochlore lattices. Above the saturation field, the energy of the magnetic moments in the external field takes predominance over antiferromagnetic interactions and stabilizes ferromagnetic alignment of all spins parallel to the field direction. The thermodynamics of the reverse phase transformation from a fully magnetized state at $H>H_{sat}$ into a partially magnetized state at $H<H_{sat}$ present a number of unusual features in frustrated antiferromagnets [4].

Reduction of the total magnetization in antiferromagnets is generally controlled by flips of individual spins. Magnetic interactions between lattice sites transform spin-flips into collective propagating excitations with a finite energy gap proportional to $H-H_{sat}$ above the saturation field. In ordinary non-frustrated antiferromagnets the gap vanishes at $H=H_{sat}$ for a specific wave-vector, which determines the ordering wave-vector of a canted antiferromagnetic structure below H_{sat}. Frustrated antiferromagnets (Kagomé, pyrochlore, garnet etc) have, in contrast, a flat momentum-independent branch of spin-flips with vanishing gap at $H=H_{sat}$. The presence of such a branch is a consequence of a macroscopic degeneracy of the ground state below H_{sat}. Close to the saturation field, corresponding low-energy excitations behave as effective paramagnetic degrees of freedom. Such emergent excitation degrees experience an effective magnetic field (H-H_{sat}). Therefore, as H approaches H_{sat} under adiabatic conditions (see inset 2), the frustrated magnet should cool down in a very similar way to an adiabatic demagnetization of an ordinary paramagnetic salt. The main difference between the two processes is that a frustrated magnet tends to reach the lowest temperature at $H=H_{sat}$, while an ordinary paramagnet reaches the lowest temperature at $H=0$. Analytic theory of the demagnetization process of frustrated magnets requires going beyond a simple harmonic approximation. It is still under development and beyond the

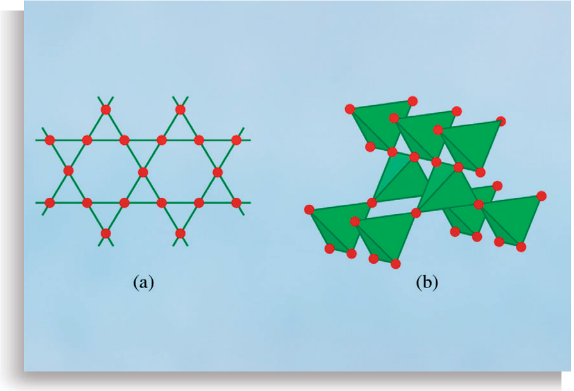

Figure 1: Geometrically frustrated lattices: Kagomé (a) and pyrochlore (b).

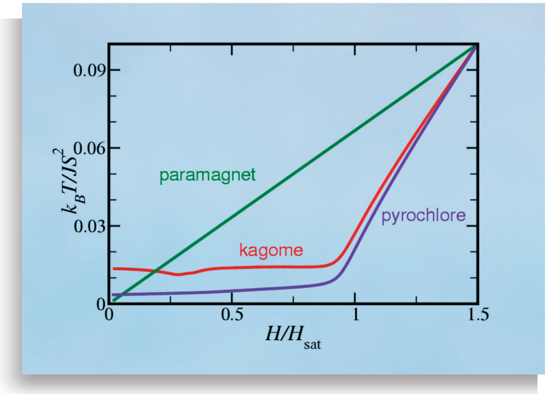

Figure 2: Temperature variation during adiabatic demagnetization of pyrochlore and Kagomé antiferromagnets. The straight line corresponds to the demagnetization process of an ideal paramagnet.

scope of this article. Instead, a numerical approach is presented here [4].

Specifically, we consider Heisenberg interactions between neighbouring spins. Large values of spins of magnetic ions in frustrated magnetic materials: $S=3/2$ (Cr^{3+}) and $S=7/2$ (Gd^{3+}) allow us to approximate quantum spins as classical magnetic moments. Under such an approximation, powerful Monte Carlo techniques can be used for simulation of large finite clusters (typically $N>1000$) in order to derive the thermodynamic behaviour of macroscopic samples. The standard Monte Carlo algorithm corresponds to simulations at a fixed temperature. We have implemented a modified algorithm, which makes it possible to numerically simulate the adiabatic process at constant entropy.

In Fig. 2 we present results for adiabatic demagnetization of two frustrated antiferromagnets in comparison with an ideal paramagnet, which has a linear dependence T/H=cst (see inset 2). The adiabatic temperature decrease for frustrated magnets is much steeper than for a paramagnet in a wide interval of magnetic fields. The temperature of a pyrochlore antiferromagnet drops by more than ten times as the field decreases from $1.5H_{sat}$ to $0.8H_{sat}$. To achieve a similar cooling with a paramagnetic salt, an applied field has to be decreased by at least a factor of ten. The predicted cooling effect should be easily observable, for instance, in $Gd_2Ti_2O_7$, where $H_{sat}=6.5$ T and $JS^2/k_B=3.7$ K. The obtained results suggest that frustrated antiferromagnets with suitable saturation field values may be utilized as alternative refrigerant materials.

1. Geometrical frustration

Let us consider magnetic moments located at the vertices of equilateral triangles and coupled antiferromagnetically (neighbouring moments have anti-parallel orientations). This coupling scheme cannot be satisfied simultaneously for all these moments (see figure). This illustrates the so-called geometrical frustration.

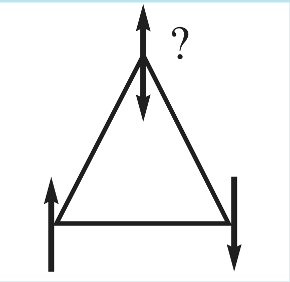

2. Adiabatic demagnetization

The adiabatic demagnetization technique based on the magneto-caloric effect has been successfully used to reach temperatures in the sub-kelvin range. During an adiabatic process, i.e. for a thermal isolation from environment, the total entropy of the system remains constant. Paramagnetic salts, which are standard refrigerant materials for low temperature cooling, consist of non-interacting magnetic moments (spins). The two energy scales are the Zeeman energy and temperature. Therefore, the entropy of an ideal paramagnet depends on field and temperature via H/T. This means that during adiabatic demagnetization, temperature of a paramagnetic salt decreases at best linearly with magnetic field.

[1] A. P. Ramirez in Handbook of Magnetic Materials Vol. 13, edited by K.H.J. Buschow (Elsevier, Amsterdam, 2001) p.423.
[2] J. T. Chalker, P. C. W. Holdsworth, and E. F. Shender, Phys. Rev. Lett. **68,** 855 (1992).
[3] M. E. Zhitomirsky, A. Honecker, and O. A. Petrenko, Phys. Rev. Lett. **85,** 3269 (2000).
[4] M. E. Zhitomirsky, Phys. Rev. B **67,** 104421 (2003).

Contact: mzhitomirsky@cea.fr

LINKING *AB INITIO* AND MONTE-CARLO CALCULATIONS

**D. Caliste, Th. Deutsch,
F. Lançon, and S. Goedecker**

Service de Physique des Matériaux
et des Microstructures (SP2M), DRFMC

Fast algorithms allow the behaviour of materials at the atomic level to be simulated on powerful computers, and their macroscopic properties to be deduced. Large systems with low concentration of alloying atoms or defects can henceforth be studied. The properties of high quality materials like silicon and its alloys (SiGe, SiGeC) are therefore now accessible to simulation.

Des algorithmes rapides permettent de calculer le comportement des matériaux à l'échelle atomique, et d'en déduire des propriétés macroscopiques. On peut désormais étudier de grands systèmes comprenant une faible densité d'atomes d'alliage ou de défauts, donnant accès aux propriétés de matériaux de haute qualité tels le silicium et ses alliages.

I. INTRODUCTION

In atomic simulation, tools are adapted to the number of particles of the system. Methods simulating thousands of atoms generally rely on inter-atomic potentials. The atomic interaction is then simplified to the interaction between couples of atoms, described by a potential energy function. The parameters are fitted on experimental data, or derived from calculations performed on reduced sets of atoms. Large numbers of atoms can then be efficiently addressed, at the expense of accuracy, and provided that the inter-atomic potential between all couples of different atoms in the compound is known…

We are developing methods to circumvent these drawbacks. One is based on *ab initio* calculations, solving (obviously with some degree of approximation) the basic Schrödinger equation rather than fitting data. This method directly addresses the electron orbitals, it is more accurate, and furthermore applicable to any atomic composition. It is also very expensive and therefore limited to systems of a few hundred particles. The second method is the widely used Monte Carlo simulation. Using a model that gives the probability of all elementary processes acting on each particle, an algorithm randomly picks one of these processes according to its probability, changes the system configuration, again picks a process, and so on… thus simulating the evolution of the system. In this way, systems comprising millions of atoms can be

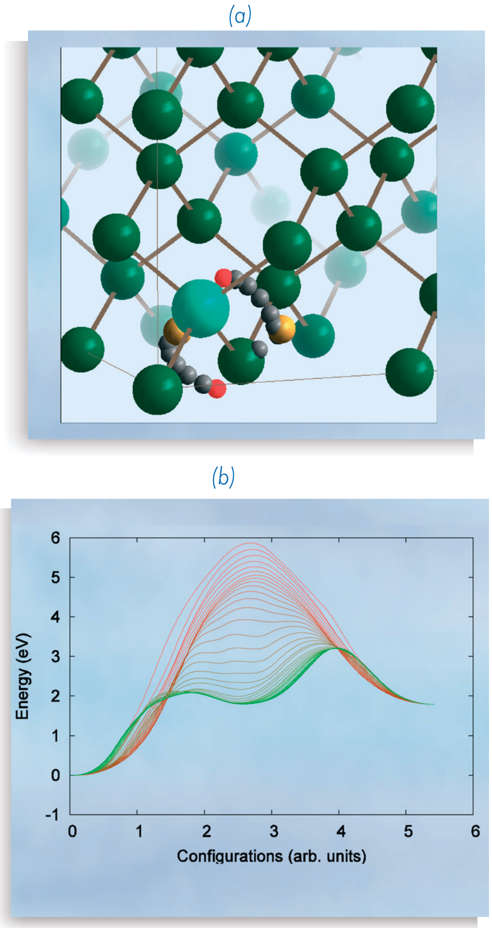

Figure 1: (a): Calculation of the energy barrier associated to the process exchanging a germanium atom with a silicon neighbour (light green: Ge - dark green: Si - yellow: intermediate position - red: "pass" position). Both atoms move simultaneously, starting from the initial green position, passing through the yellow and red positions, where the system switches over the "pass" towards the final valley. (b): The red to green curves correspond to successively calculated paths. Only 3/4 of the movement is shown, from the initial position (left) to the "pass" position (right). The red curve represents the energy along the path at the beginning of minimization. The green one represents the final optimized path.

simulated. The accuracy is limited by the accuracy in describing elementary processes, and thus the choice of the model is of crucial importance. Our goal is to build a model from accurate *ab initio* calculations.

With this strategy, we plan to simulate atomic movements called kinetic events, in the SiGeC alloy, a compound of major technological interest. We present here an improved method to calculate the energy barriers governing elementary processes, and the derivation of macroscopic quantities with Monte Carlo simulations, taking advantage of these *ab initio* calculations.

II. COMPUTING BARRIER ENERGIES

The energy needed to go from one atomic configuration to another is called the energy barrier: it governs kinetic events. While the stable configurations (including substitutions of atoms) are generally known, the energy needed along the path in between is generally unknown. For simulating such processes we need to explore all the barriers involved during the movement. For instance, simulating the diffusion of Ge atoms in SiGe requires the energy needed to move a Ge atom from one substitutional site to another to be known.

We use a method called "nudged elastic band" that finds a path from one configuration to another within different conditions of slope of the energy variation, just like a walker could do for finding a pass from one valley to another. The program starts by selecting intermediate atomic positions corresponding to a tentative movement. Using accurate *ab initio* calculations, it computes forces applied on atoms in each position and moves them accordingly. It computes forces in new positions and moves atoms again, and so on, until forces decrease below a given criterion. The final path minimizes the energy barrier to be overcome during the movement (see Fig. 1). Such calculations involve large numerical resources (vectorial computers or PC clusters), but are very accurate. The number of computable barriers is limited by the time available on computers.

III. TOWARDS HIGH SCALE SIMULATIONS

We build a database of energy barriers using the above-mentioned *ab initio* calculations. During a simulation, the Monte Carlo model will pick the parameters of the different elementary processes from the database. Using such an approach we simulate vacancy movements in pure silicon with low defect concentration, illustrating the performance of the Monte Carlo algorithm.

Vacancies are expected to cluster in silicon, modifying their behaviour. However, due to their low concentration in silicon crystals, they are difficult to track experimentally. Since modern Monte Carlo methods manage large numbers of atoms, realistic low concentrations of vacancy can be dealt with. We show that the diffusion of vacancies is slowed down by a factor of several decades as soon as they meet one another (see Fig. 2). Simulation therefore confirms results that were reasonably expected but not yet quantified.

IV. CONCLUSION

These two examples illustrate the tools we have developed: we manage large systems with altogether a realistic description of elementary processes through *ab initio* calculations, and an efficient simulation of the movements of vacancies or alloying atoms by means of powerful Monte Carlo methods. These methods can now be linked for fully simulating alloys like SiGeC, in which complex phenomena such as interactions between germanium, carbon, and interstitial carbon atoms are expected.

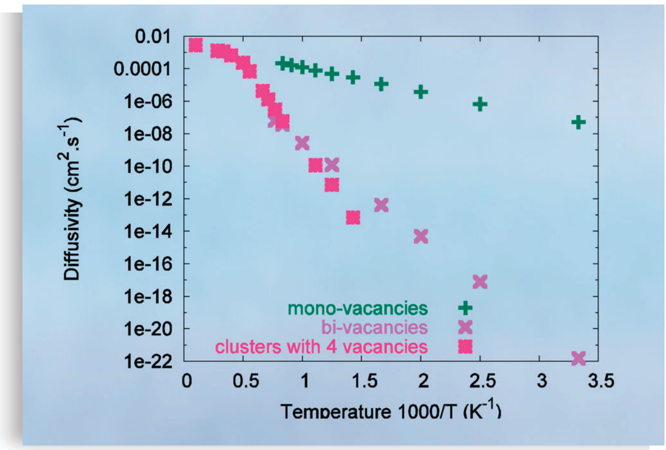

Figure 2: Diffusivity depending on temperature, calculated for vacancies and clusters with two and four vacancies in pure silicon.

Contact: dcaliste@cea.fr

WAVELETS APPLIED TO ELECTRONIC STRUCTURE CALCULATIONS

C. Chauvin*, Th. Deutsch, and S. Goedecker.

Service de Physique des Matériaux et des Microstructures (SP2M), DRFMC

Simulation enables theory and experiments to be compared or experiments to be predicted. For phenomena governed by atomic scale interactions, a key issue is solving the Schrödinger equation. Electrical properties, for instance, can then be deduced therefrom. We present a way of solving this equation, addressing systems like molecules or solids.

La simulation permet de comparer théorie et expériences ou de prévoir ces dernières. Pour les phénomènes régis par des interactions à l'échelle atomique, un point clef est la résolution de l'équation de Schrödinger. On peut alors en déduire, par exemple, des propriétés électriques. Nous présentons un moyen de résoudre cette équation, pour des systèmes tels que molécules et solides.

* * *

I. Introduction

Solving the quantum mechanical Schrödinger equation for systems of some hundreds of atoms would require huge efforts, beyond computational capabilities. The Density Functional Theory (DFT) [1] can circumvent the problem; in this framework the Kohn-Sham equations are a powerful approximation, by which the equation has to be solved for one electron. The potential acting on this electron only depends on the electron density of presence.

Mathematically the electron density is a function that must be developed into a set of functions called a *basis*. Efficiency is crucially determined by the choice of this set. We present here the *wavelet basis* that emerged during the last decade as very promising. However, once the basis has been chosen an efficient code has to be developed, especially for calculation of the electron-electron interaction potential *via* the Poisson equation.

A fast and accurate method addressing systems with hundreds of electrons contained in a 3D box is needed. As computations are performed in a discrete way, we evaluate potentials and electron density on a *mesh grid*. Rather than directly calculating the density on the real point grid, we expand it on another one where computation is more efficient. This new grid represents the coefficients of the electron density spanned on a suitable *basis set*. A good accuracy requires more grid points around nuclei where the density is larger (see Fig. 1). The complexity in solving Poisson and Schrödinger equations depends strongly on this basis set. We now face two problems: how to express the different operations simply and how to adapt the grid?

II. Choosing the basis set

Chemists first used localized basis sets, but other sets can be considered.

(i) Since the functions describing the electron density around atoms are gaussian and since it is large only near the nuclei, it seems natural to expand it on a *localized basis* set. In fact, operations to be performed on the simplified grid are too expensive, especially solving of the Poisson equation.

(ii) The *plane waves basis* describes well quasi-free electrons in solids, but has no physical meaning in the case of molecules or nanostructures. The coefficients on this basis are derived through a Fourier transform, optimizing solving of the Poisson equation. However the grid must be regular all over the box and it must be fine if good accuracy is required. Long calculations are thus performed in almost empty regions, leading to a high computational cost.

(iii) The *wavelet basis* [2]. The density is expressed on an adaptive grid: the chosen wavelets are localized at points where a large density is expected (see Fig. 1). This method emerged in the 80's, and intuitively appears as an efficient way to solve the

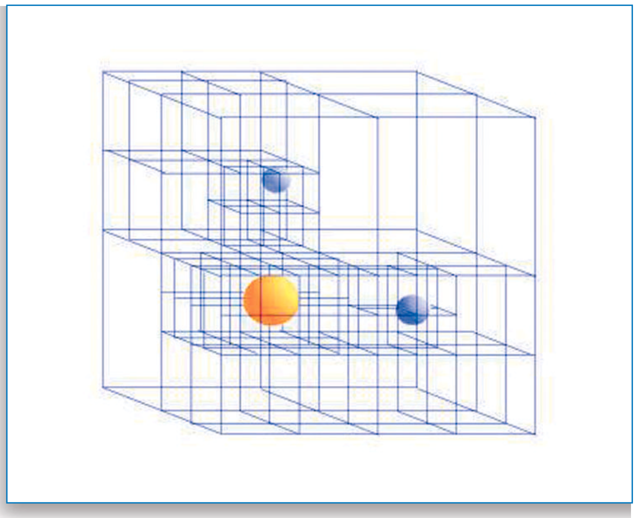

Figure 1: Example of a 3D system: a 3-atom molecule and a corresponding adaptive mesh grid.

Schrödinger equation. One key is to get a good solver for the Poisson equation. While the wavelets cannot compete on a regular grid with plane wave methods, the fact that they are intrinsically well localized both in real and in frequency space (see Fig. 2) leads to a reasonable result when details of the electron density are needed around atoms [3].

III. CONCLUSION

Development of the wavelet basis method gives promising results [3]: we expect the code to compete with traditional methods. We are presently addressing the design of a general solver for the Schrödinger equation. Next we will be implementing an adaptive scheme, automatically generating grids for more general problems.

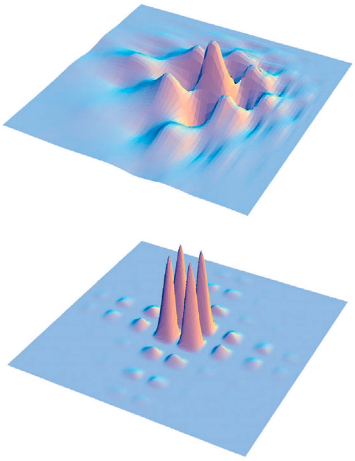

Figure 2: Sections of a typical 3D wavelet basis function (8-degree Daubechies wavelet), in real space (up) and frequency space (down).

What is wavelet analysis?

Wavelet analysis was created in the 80's for addressing various problems, from theory in mathematics and physics to engineering applications. One famous success of wavelets is the JPEG 2000 compression algorithm.

Previous compression algorithms used a discrete cosine transform. A standard 640 by 480 pixel image was for example divided into blocks of 8 by 8 pixels. Applying the transform on each block of 64 numbers gives 64 other coefficients, which are then ordered in a decreasing way. Keeping only the 8 most significant coefficients and applying the inverse transform, an image with only a few coefficients is restored, obviously at the expense of quality. The resolution of the compressed image was in fact not sufficient, especially at the edges of blocks.

Wavelet analysis offered a decisive improvement: rather than dividing the image into blocks of fixed size, wavelet analysis addresses the different scales of the image. Consider the photography of a tree: the main features are the trunk, boughs, and leaves. On a finer scale, the trunk roughness, and each leaf composing the green form can be detailed; on a still finer scale, the leaf veins can be distinguished. Correspondingly, wavelet analysis will decompose the image from the coarsest scale (the tree in general) to the finest one (each leaf). Suppressing irrelevant finest details such as small variations of the sky, trunk, and leaves, the essential information is kept at a medium resolution. In this way an efficient compression is achieved, while saving a reasonable quality of the image. Wavelet analysis is therefore well suited to data processing, but it is also very efficient in scientific calculation, as it consists of convolutions with reasonably short filters.

---

* present address: claire.chauvin@imag.fr

[1] W. Kohn and L. J. Sham, Phys. Rev. A **140,** 1133 (1964).
[2] I. Daubechies, *Ten lectures on wavelets*, CBMS-NSF Regional Conferences Series in Applied Mathematics Vol 61 (SIAM, Philadelphia/USA, 1992).
[3] S. Goedecker and C. Chauvin, J. Theor. Comput. Chem. **2,** 483 (2003).

Contact: tdeutsch@cea.fr

A FOURFOLD COORDINATED POINT DEFECT IN SILICON

S. Goedecker, Th. Deutsch, and L. Billard

Service de Physique des Matériaux
et des Microstructures (SP2M), DRFMC

Point defects result from the lack (vacancy), insertion (interstitial), or displacement (Frenkel pair) of an atom in a solid. They are considered as the basic defects in silicon. We predict a new point defect in silicon, fourfold-coordinated and lower in energy than the others.

Les défauts ponctuels résultent du manque (lacune), de l'insertion (interstitiel) ou du déplacement (paire de Frenkel) d'un atome dans le réseau. Ils sont considérés comme les défauts de base du silicium. Nous prédisons l'existence d'un nouveau défaut ponctuel, tétra-coordonné et d'énergie de formation plus faible que les autres.

Due to their technological importance, point defects in silicon are among the most studied physical systems. The experimental evidence of point defects buried in bulk is difficult, leading experimentalists to use rather indirect methods. In parallel, simulations of defects have been performed at various levels of sophistication. The generally accepted conclusion of all these studies is that vacancies and self-interstitials are the basic point defects in silicon.

Such defects result from taking out or adding atoms to the crystal. Therefore the fourfold coordination is destroyed, leading to rather high defect formation energy. In addition there is another point defect, conserving the number of atoms, the Frenkel pair, consisting of a vacancy and an interstitial. Its formation energy is also large since again bonds are broken (see Fig. 1).

Using state of the art plane wave density functional theory calculations (DFT) we found a new defect that, in contrast to other point defects, conserves the fourfold coordination and will therefore be called the fourfold coordinated defect (FFCD). Whereas the finding of classical point defects was based on simple symmetry considerations, the discovery of this new point defect was made possible by new algorithmic developments. The configurational space was systematically explored using a modified basin hopping method and an inter-atomic silicon potential. The most promising configurations were then refined with a plane wave electronic structure code developed by a consortium in which we participate [1, 2]. Figure 2 shows the novel defect configuration.

We have summarized in Table 1 the total energy of all low energy defects calculated for intrinsic silicon by various authors. In addition we have included a low energy Frenkel pair. We did not include the tetrahedral interstitial and caged interstitial that were found higher in energy and metastable. The 2.4 eV formation energy of the FFCD is clearly lower than the formation energy of all other known point defects both in intrinsic and doped silicon. The bond length and angle do not significantly deviate from the bulk values. Whereas the bond length and angle in the bulk are 2.35 Å and 109 degrees, they respectively vary from 2.25 to 2.47 Å and from 97 to 116 degrees for the bonds formed by the two (red) defect atoms. In order to annihilate the defect, two bonds have to be transiently broken, corresponding to a barrier energy of 0.57 eV. The FFCD defect is close to the so-called "bond defect", the configuration of which was inferred from less accurate tight binding simulations of bulk silicon [3]. We found the precise configuration of the stable defect and calculated its formation energy for the first time.

FFCD	Frenkel	X interstitial	H interstitial	Vacancy
2.42	4.32	3.31	3.31	3.17

Table 1: Formation energy in eV of the low energy point defects.

Due to the properties of this new defect, it is hardly detectable experimentally, and as a matter of fact it was not detected until now. We have explored the possible rea-

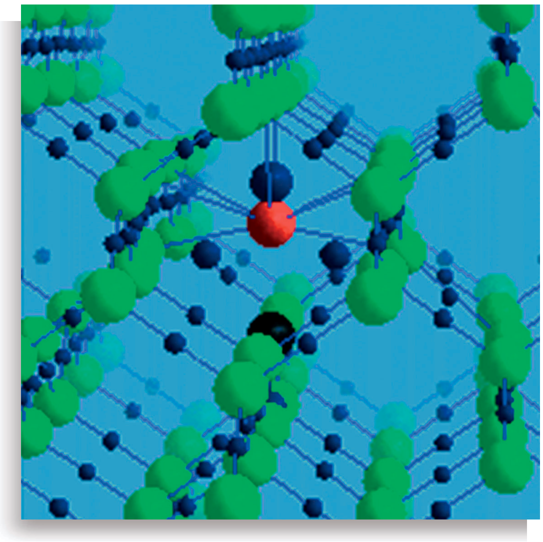

Figure 1: Frenkel pair defect in silicon. Green spheres: Si atoms - red sphere: atom in new position - black sphere: vacancy (former atom position) - small blue spheres: covalent bonds - large blue spheres: perturbed bonds.

sons for this situation. Firstly, because of the perfect fourfold coordination, no unpaired electrons exist that could be detected with Electronic Paramagnetic Resonance (EPR) and Electron Nuclear DOuble Resonance (ENDOR) experiments. Secondly the presence of electronic levels within the gap, which could be evidenced through Deep Level Transient Spectroscopy (DLTS), also seems unlikely. To confirm this point we calculated the Highest Occupied Molecular Orbital (HOMO) and Lowest Unoccupied Molecular Orbital (LUMO) splitting. In fact the band structure is much less disturbed by the FFCD than by the other defects. Finally the FFCD spectrum is insensitive to the doping level whereas the other spectra are strongly influenced *via* various Jahn-Teller distortions because of their orbital degeneracy. Therefore the presence of the defect could not be detected through its influence on dopants. Rutherford backscattering experiments on light ion implanted silicon samples give energy spectra that can be fitted on the basis of defects of this type, but cannot unambiguously confirm a precise configuration.

In fact, due to its low formation energy, this defect is probably generated during implantation of light ions in silicon. The annihilation barrier energy leads to a relatively short lifetime at room temperature. However, during its lifetime, the FFCD can either promote the migration of self-interstitials or dopants, or cluster with other FFCD, leading to more stable configurations, which could in turn play an important role in room-temperature amorphisation of silicon during the implantation process. We are continuing the track, reviewing and calculating possible experimental signatures of the defect, and are also simulating more extended defects using the FFCD as a building block.

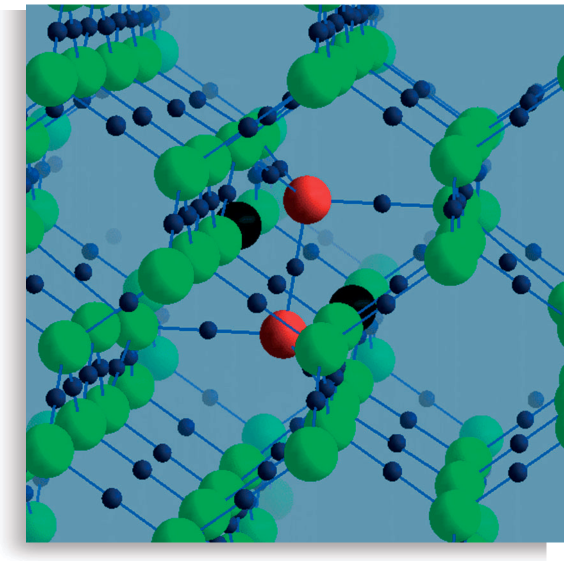

Figure 2: FFCD defect in silicon. Green spheres: Si atoms - red spheres: atoms in new positions - black spheres: empty lattice sites (former positions) - small blue spheres: covalent bonds.

[1] CPMD Version 3.3 developed by J. Hutter, A. Alavi, T. Deutsch, M. Bernasconi, S. Goedecker, D. Marx, M. Tuckerman and M. Parrinello, Max-Planck-Institut für Festkörperforschung and IBM Zürich Research Laboratory (1995-1999).

[2] S. Goedecker, T. Deutsch, and L. Billard, Phys. Rev. B **88,** 235501 (2002).

[3] F. Cargoni, C. Gatti, and L. Colombo, Phys. Rev. B **57,** 170 (1998).

Contact: tdeutsch@cea.fr

INCOMMENSURATE INTERFACES IN METALS

F. Lançon

Service de Physique des Matériaux
et des Microstructures (SP2M), DRFMC

The interface between two crystals is incommensurate when the ratio of their periodicities along the interface is an irrational number. We have shown that such interfaces in mono-atomic metals including gold and copper can have a specific behavior. Hypo-friction of the interface sliding and triple-line reconstruction are considered here.

Une interface entre deux cristaux est dite incommensurable lorsque le rapport des périodicités le long de l'interface est un nombre irrationnel. Nous avons montré que de telles interfaces dans les métaux purs comme l'or ou le cuivre ont des propriétés particulières. Nous nous intéressons ici à l'hypo-friction lors du glissement de l'interface et à une reconstruction de ligne triple.

Solid bodies are generally constituted by microscopic crystalline grains separated by interfaces called grain boundaries. While the general solid-state theory depicts the properties of single crystals, the properties of poly-crystalline solids are largely influenced by the presence of these boundaries, which affect features like mechanical behavior, electrical and thermal conductivity, diffusion of impurities... The advent of nanomaterials made of nanometer-sized grains further amplifies the role of the boundaries. Most of the studied grain boundaries deal with lattices having a common period, a multiple of the periods of both crystals. However in most of the real cases there is no such common periodicity; the interface is then called incommensurate. Usually a periodic structure is found that describes the properties of the interface with rather good accuracy, but sometimes, as illustrated in this paper, the incommensurability has specific consequences.

A simple incommensurate structure has been found by high-resolution electron microscopy in gold [1] and aluminium. It is a grain boundary between two face centered cubic (fcc) crystals. In order to visualize the grain boundary plane, a cube can be imagined cut in two prisms as shown in Fig. 1. If one half is rotated 90° with respect to the other, its face diagonal (length $\sqrt{2}$) comes along the edge of the other half (length 1). The crystalline grains have a common axis such that atoms viewed from this direction form rectangles with edges proportional to 1 and $\sqrt{2}$. The first grain has the edge of length 1 along one side of the interface (x axis); the second grain is rotated through 90° with the $\sqrt{2}$ edge coming along this x axis. Because $\sqrt{2}$ is an irrational number, the interface cannot be periodic along x. Close to the interface, atoms of each grain have positions perturbed by the atoms of the other grain. As a result, the interface has a complex incommensurate structure.

This structure is non periodic but, by adding a virtual fourth dimension to the usual space, it can however be represented by periodic sets of lines in a 4D hyperspace (see Fig. 2). The actual atomic coordinates (0D features) are given by the intersections of so-called "atomic lines" (1D) with the physical space (3D). This theoretical tool, already used in the field of quasi-crystals, condenses

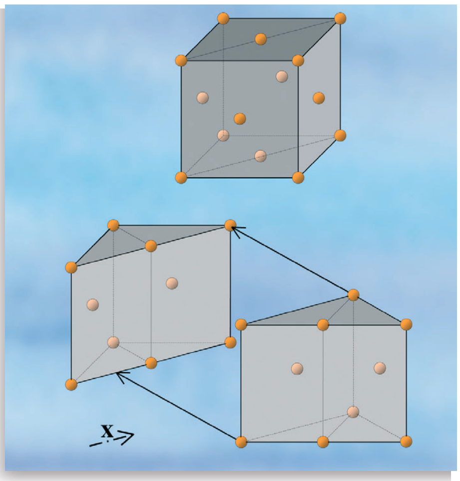

Figure 1: A basic fcc cube (top) is cut into two prisms. One (bottom right) is rotated with respect to the other (bottom left), showing the incommensurability of the edges.

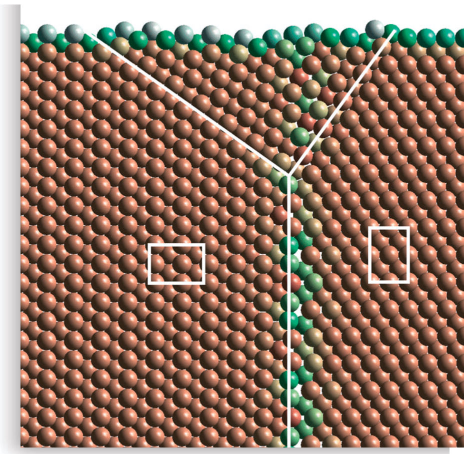

Figure 3: Interaction of the grain boundary with the surface in copper. White rectangles: orientation of the grains. At the surface, the chevron domain replaces the grain boundary energy by a more diffuse energy, which is globally lower.

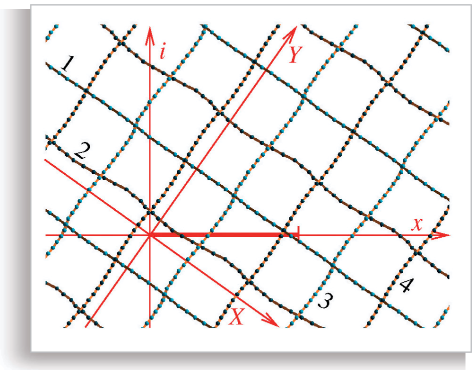

Figure 2: Incommensurate interface viewed in a hyper-space. Atoms are represented by "atomic lines" when a virtual direction i is added. The intersections of these lines with the real x-axis give the x positions of the atoms.

all the information on the atomic positions of each atomic layer from -∞ to +∞ inside a finite and small square unit cell.

Based on this analysis of the structure, and using atomistic simulations, we have predicted that this ideal 90° incommensurate interface can have the surprising property of zero static friction. S. Aubry originally found a similar behavior in a 1D atomic chain model: he proved that a chain embedded in an external periodic potential may be stuck ("pinned") or freely sliding ("unpinned"), depending on the interactions [2]. We have found the first example of such a property in a real material by investigating the case of gold. We show that the two possible states, pinned or unpinned, exist for the 90° grain boundary [3], and that the dynamical property of sliding is related to the topology of the atomic lines defined in the 4D framework. If the atomic lines are continuous, one grain can slide along the other without an energy barrier: the grain boundary has the property of hypo-friction. If the lines are discontinuous the grains are pinned to each other, just like in standard periodic grain boundaries.

Another interesting situation arises when the grain boundary interacts with the free surface of the material. We have evidenced a new behavior corresponding to a line reconstruction at the intersection of this boundary with the free surface. The intersection line is transformed into a "wire" with a cross section of a few nanometers that was observed by electron microscopy and explained by our simulations [4]. The chevron-like triangular domain shown in Fig. 3 results from the balance between two energy terms: one is the energy of the grain boundary area that has been replaced, and the other is the energy of the stacking faults present in the domain, almost transformed from face centred cubic to hexagonal close packing. A detailed analysis of these terms gives the conditions for its stability [5]. The calculations were confirmed by the experimental results, for instance the reconstruction is present in gold but not in aluminium.

At the fundamental level, these studies help our understanding of the interplay between crystalline surfaces. The properties of this type of interfaces have implications on grain dynamics: this new type of sliding at the interface can increase plasticity by several orders of magnitude, while the line reconstruction brings a new mechanism efficiently pinning the interface at the surface.

Acknowledgements

The author acknowledges the hospitality of the National Center of Electron Microscopy (NCEM) during a research leave at the Berkeley National Laboratory and thanks his collaborators U. Dahmen and T. Radetic. ▮

[1] F. Lançon, J.-M. Pénisson, and U. Dahmen, Europhys. Lett. **49,** 603 (2000).
[2] S. Aubry, Solid State Science Vol. 8 (Springer-Verlag, Berlin/Germany, 1978) p. 264.
[3] F. Lançon, Europhys. Lett. **57,** 74 (2002).
[4] T. Radetic, F. Lançon, and U. Dahmen, Phys. Rev. Lett. **89,** 85502 (2002).
[5] F. Lançon, T. Radetic, and U. Dahmen, Phys. Rev. B **69,** 172102 (2004).

Contact: flancon@cea.fr

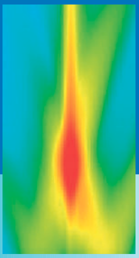

SIMULATION OF GRAZING INCIDENCE SMALL ANGLE X-RAY SCATTERING TWO-DIMENSIONAL IMAGES

F. Leroy, G. Renaud, R. Lazzari*, and C. Revenant

Service de Physique des Matériaux et des Microstructures (SP2M), DRFMC

Grazing Incidence Small Angle X-ray Scattering (GISAXS) is a powerful tool to analyze the topography and morphology of nano-objects deposited on or buried below surfaces. Extracting quantitative information requires approximations to the general scattering theory, which are discussed on facetting of W(111) surfaces into nanopyramids.

La diffusion aux petits angles en incidence rasante (GISAXS) est une méthode puissante pour analyser la topographie et la morphologie de nano-objets déposés sur ou enterrés sous une surface. L'accès à l'information quantitative nécessite des approximations à la théorie générale de la diffusion, discutées dans le cas du facettage de surfaces de W(111) en nanopyramides.

GISAXS is becoming a common tool, at third generation synchrotron sources, to characterize the shape, size, and ordering of nanoparticles deposited on, or buried below, a surface. It can even be used *in situ*, during the elaboration of nanostructures [1]. As illustrated in Fig. 1, the incident X-ray beam impinges on the sample at a grazing incident angle, and the scattered intensity is recorded perpendicularly to the beam with a two-dimensional detector. Nanometer-sized non-homogeneities of the electron density or nanostructures on the surface scatter the X-rays at small angles. The figure shows how X-rays scatter on the nano-facets of small triangular pyramids, grown on a W(111) surface after annealing of a 1ML Pt deposit [2]. In the Born approximation (BA) single scattering of X-rays is assumed. The GISAXS image is thus the squared Fourier transform of the real space topography: the smaller the lateral (resp. vertical) size of the nano-objects, the larger the extent of the scattering parallel (resp. perpendicular) to the surface. Qualitative features can then be deduced from experimental data. First the three-fold symmetry of the pattern through the rotation of the sample in its plane proves the three-fold symmetry of the nano-pyramids. Next we observe scattering rods at an angle of 18.6° (Figs. 1 and 2a) with respect to the surface. Since a two-dimensional facet in real space yields a perpendicular one-dimensional rod in reciprocal space, we infer the existence of [112] facets from this angle.

Extracting quantitative information such as the facet size and pyramid height requires a theoretical treatment. A first complication arises from the very small incident grazing angle α_i: not only the incident beam is present above the surface (and thus scattered by the objects), but the specular reflected beam also is, scattered with similar amplitude. The additional term, multiplied by a reflection coefficient (~1 for small α_i) and shifted perpendicularly to the surface by an exit angle $\Delta\alpha_f = 2\alpha_i$, interferes with the direct scattering term. This leads in Fig. 1 to two parallel rods shifted perpendicularly to the surface, while the single scattering approximation predicts only one. Thus, for simulating the data, we use the Distorted Wave Born Approximation (DWBA), which takes "multiple scattering" into account. A second complication arises from the fact that the islands are not identical, displaying a statistical distribution of size and shape. The only tractable approach is then to compare with models that take the physics of the growth into account.

A common approach is the Local Monodisperse Approximation (LMA). It is assumed that neighboring islands locally have the same size, and that zones with islands of different sizes are separated by distances larger than the coherent length of the beam. Waves scattered by different zones are then added incoherently, and the total intensity is the sum of intensities scattered by these zones. This does not however account for frequent situations where islands of rather different size are close to each other, thus scattering coherently.

The decoupling approximation (DA) addresses islands of different size and distances in the same zone. It assumes decoupled distributions: the size of an island does

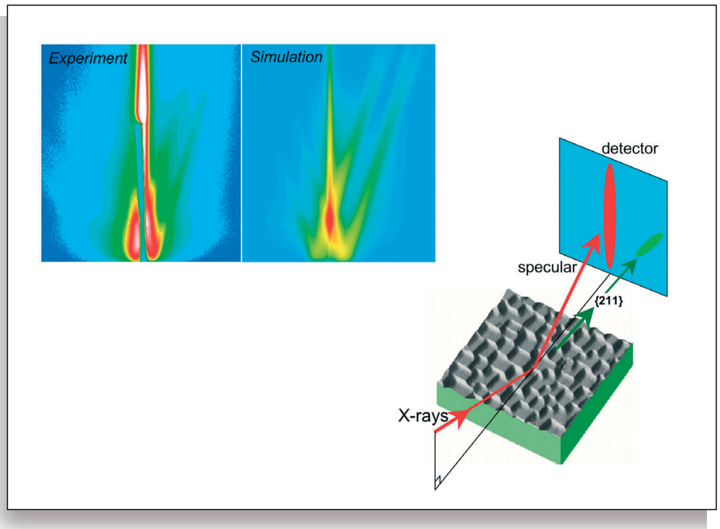

Figure 1: Schematic of a GISAXS experiment, and experimental GISAXS image recorded on a nanofacetted W(111) surface. The horizontal is parallel to the surface. The incident and reflected beam, as well as the specular scattering rod, are hidden by a beam stop. The GISAXS has three-fold symmetry on rotation of the sample with respect to a vertical axis, perpendicular to the surface.

not depend on the size or position of neighbors. This approximation does not take into account various correlations between the sizes and/or the separation of neighboring islands. In fact the processes (growth or coalescence) leading to an island larger than the average also lead to a larger depletion area around it, in turn making the neighboring islands nucleate and grow farther. This yields a positive correlation between island sizes and separations, and generally a positive correlation between sizes of neighboring islands.

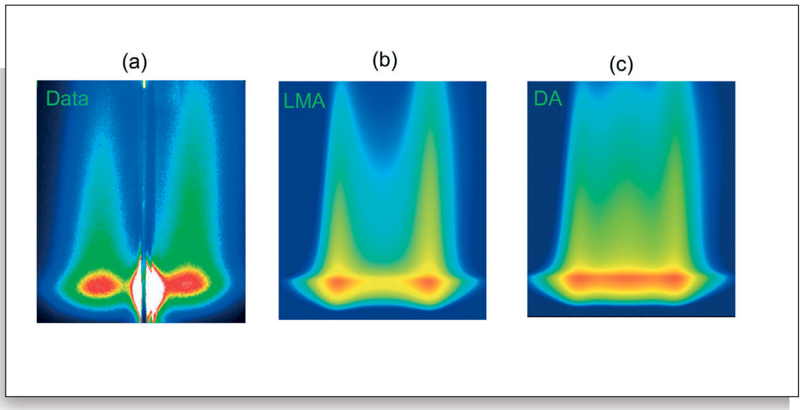

Figure 2: (a): GISAXS data of small correlated nanopyramids of the nanofacetted W(111) surface. (b) and (c): Simulations using the Distorted Wave Born Approximation (DWBA) plus two further approximations LMA (b) and DA (c).

We have developed a software package called IsGISAXS [4] to simulate, analyze and fit GISAXS data for a large variety of nanoparticle assemblies, either embedded below or sitting on a surface. Particles may have the various shapes experimentally observed, with different lateral and vertical size distributions. They may be located on the node of perfect or disordered crystals with several variants related by symmetry, or distributed in a disordered way, characterized by a specific particle-particle pair correlation function. Within the above two approximations, the program enables the experimental GISAXS data to be fitted and simulated in almost all situations encountered up to now, as exemplified in Fig. 2 where LMA and DA were used to simulate GISAXS data on small (~10 nm) correlated nanopyramids. The LMA describes the data better, as seen in the figure. However electron microscopy shows that the islands are not locally monodisperse. This points the limits of the generally adopted approximations; we are now developing more sophisticated models to take diffuse scattering of X-rays on correlated systems into account [5].

---

* present address : Groupe de Physique du Solide, Univ. Paris-6

[1] G. Renaud, R. Lazzari, C. Revenant, A. Barbier, M. Noblet, O. Ulrich, F. Leroy, J. Jupille, Y. Borensztein, C. R. Henry, J.-P. Deville, F. Scheurer, J. Mane-Mane, and O. Fruchart, Science **300,** 1416 (2003).
[2] J. J. Kolodziej, T. E. Madey, J. W. Keister, J. E. Rowe, Phys. Rev. B **65,** 75413 (2002).
[3] C. Revenant, F. Leroy, R. Lazzari, G. Renaud, and C. R. Henry, Phys. Rev. B **69,** 035411 (2004).
[4] R. Lazzari, J. Appl. Cryst. **35,** 406 (2002).
[5] F. Leroy, R. Lazzari, and G. Renaud, Acta Cryst. A (2004) in press.

Contact: grenaud@cea.fr

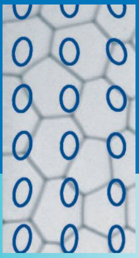

SOLIDITY OF LIQUID FOAMS

M. Aubouy

Service des Interfaces et des Matériaux
Moléculaires et Macromoléculaires
(SI3M), UMR SPrAM 5819, DRFMC

Liquid foams have wide-ranging industrial applications but their flow remains largely an unsolved physical problem. This is because it combines elastic, plastic, and viscous responses. We have devised an experimentation which, together with a careful theoretical analysis, shed some light on its uncommon features.

Les mousses liquides trouvent de nombreuses applications industrielles mais leur écoulement reste largement incompris en physique, car il associe des comportements à la fois élastiques, plastiques et visqueux. Nous avons construit une expérience qui, grâce à une théorie appropriée, permet de mieux comprendre ses caractéristiques peu communes.

In the XXth century, physics produced multiple discoveries at the forefront of our technological capacities in the aim to push forward their limits. Yet everyday life is still a source of exciting issues, and amazing discoveries are sometimes within the reach of whoever simply scrutinizes our ordinary surrounding. The subject of liquid foams belongs to this family, and naive questions do not always have definitive answers. In particular, we are used to separating materials into solids and liquids: what about foams? Clearly this is a solid if one recalls that shaving foam remains persistently on the skin. However, foam flows easily in the fire-extinguisher. Soon we realize that this is an extraordinarily complicated common material. Physicists call it a "complex fluid".

In terms of fundamental physics, we are looking for the mechanical constitutive law which relates the applied force to the resulting or effective deformation (or conversely). Formulating such laws has been a query of physicists for many centuries, which resulted in two brilliant intellectual achievements: namely the theory of elasticity and hydrodynamics, which respectively define and theorize elastic solids and viscous liquids. But, in spite of their considerable successes, these theories are unable to account for the flow behaviour of large categories of materials: foams, micro-emulsions, pastes, slurries, concentrated emulsions, granular materials…

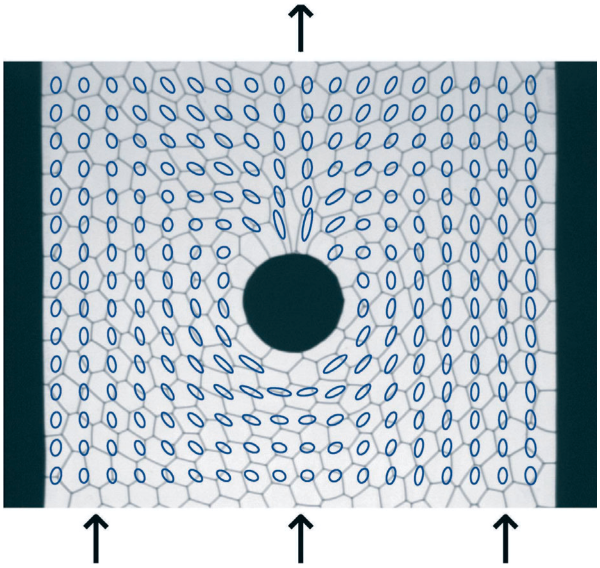

Figure 1: Instantaneous image of a two-dimensional quasi-static flow of foam around a circular obstacle (actual size: 10 cm x 8 cm). We superimposed the local determination of the statistical strain tensor represented by the solid ellipses and characterizing the effective deformation on each bubble [1].

In this list, foams are remarkable. This is because if we squeeze a liquid foam between two glass plates (to form what we call a 2d-foam) we are in a position to observe both the microscopic scale (the bubbles), and the macroscopic scale (the bulk flow). Accordingly, there is no hidden variable here, which makes it a model system for studying complex liquids.

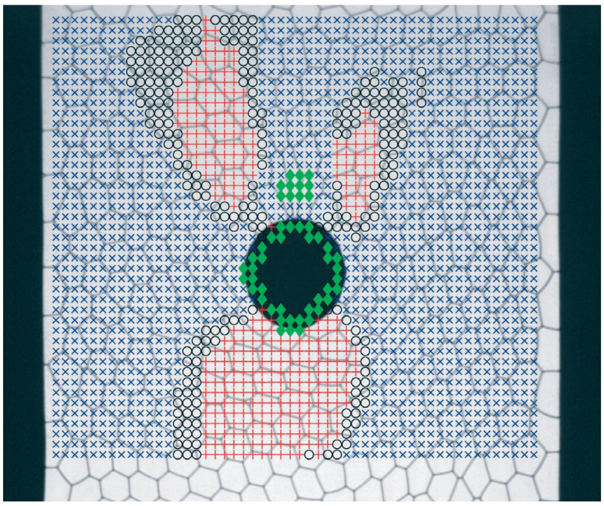

Figure 2: Our analysis of effective local strain reveals the presence of a wake around the obstacle [2].

As shown in Fig. 1, we devised an experiment where a 2d liquid foam is forced to flow around a circular obstacle. But how do we estimate the effective deformation (strain tensor)? Presumably, the difficulty is better understood if we compare the foam to a piece of rubber. Suppose we pull an elastic band from rest: the variation of its length quantifies the applied deformation (equal to the effective deformation), and the force we experience is proportional to it, since the elastic band returns to its initial state when our effort is released. In contrast, when we squeeze a piece of foam in our hands, we soon feel that the resistance does not increase proportionally to the applied deformation. For instance, the material relaxes to an intermediate state: not the initial state! Accordingly, we have to distinguish the effective deformation from the applied deformation; one strain tensor does not enable the overall deformation of the material to be characterized.

As a matter of fact, this is a major conceptual step away from both the theory of elasticity and hydrodynamics, for which it is assumed that both deformations coincide (the affine hypothesis). We found an operational definition for the effective deformation that we called the statistical strain. This is a tensor that we represent by an ellipse such that the principal axes are proportional to the eigen-vectors of the local field of deformation. The pertinent scale for foams is the bubble size and the overall deformation has to be discretized at this mesoscopic scale.

We are then in a position to measure for the first time both the stress and effective strain on each bubble. Since the flow is inhomogeneous, a single image displays the complete mechanical constitutive law. Among other results, our analysis reveals the presence of a wake that was invisible to the eye (see Fig. 2 and reference [2]).

Yet a lot remains to be done. Now that we have found the proper conceptual tools, we aim at describing the whole range of mechanical responses: elastic, plastic, viscous flow. Because foams are strongly non-affine materials, these researches belong to the emerging field of "sub-continuum mechanics" (i.e. mechanics when the continuum medium hypothesis no longer holds). This is a field of great interest for the CEA since foams are used as cleaning product for radioactive contamination or as a shock damping material after ignition of a nuclear weapon (AIRIX experiment). This is also very interesting for the manipulation of nano-objects, for which all the classical assumptions of elasticity fail.

In his novel The Alchemist, Paulo Coelho tells the story of a boy who makes an extraordinary journey in a pursuit to find a fabulous treasure. He eventually finds it precisely at the place where he was when the story began. Wouldn't it be a nice story indeed if the foams we used to play with as a child should provide us with answers to long-outstanding intellectual issues? Presumably, we needed that journey to find this out, the narrator would say.

ACKNOWLEDGEMENTS

I wish to thank F. Graner and C. Quilliet for their enthusiastic collaboration.

---

[1] M. Aubouy, Y. Jiang, J. A. Glazier, and F. Graner, Granular Matter **5,** 67 (2003).

[2] M. Asipauskas, M. Aubouy, J. A. Glazier, F. Graner, and Y. Jiang, Granular Matter **5,** 71 (2003).

Contact: maubouy@cea.fr

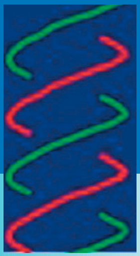

FROM DNA CHIPS TO STEALTH LIPOSOMES: BIOTECHNOLOGY-INSPIRED THEORY

A. Buhot[a], E. B. Zhulina[b] and A. Halperin[a]

a: Service des Interfaces et des Matériaux Moléculaires et Macromoléculaires (SI3M), UMR SPrAM 5819, DRFMC
b: Institute of Macromolecular Compounds, Russian Academy of Science, St. Petersburg

Two examples of theories motivated by biomedical applications illustrate the role of theory in clarifying design parameters for biotechnology. One concerns the performance of DNA chips. The second involves controlled release of drugs by stealth liposomes incorporating lipids functionalized by neutral polymers.

Deux exemples illustrent le rôle de la théorie dans le domaine de la biotechnologie. Le premier concerne l'absorption d'ADN sur des biopuces et le deuxième concerne l'étude du rôle d'un polymère neutre dans la protection contre une dégradation enzymatique d'un vecteur thérapeutique appelé liposome furtif.

It is too early to judge the utility of theory to biotechnology. However, the examples discussed below support the reverse claim: biotechnology is a source of interesting problems for theory. To illustrate their "flavor" we will discuss two examples: DNA microarrays ("DNA Chips") and stealth liposomes (SL). The first is an analytical technique of great importance to molecular biology and medicine. The second is a drug delivery vehicle for cancer therapy.

I. DNA CHIPS

DNA chips comprise a multitude of "spots". Each consists of numerous, terminally anchored, single-stranded DNA chains (ssDNA) of short length referred to as "probes". They are used to analyze the composition of solutions comprising a mixture of short ssDNA of unknown sequence known as "targets". In a typical setup fluorescent tags label the targets. The targets hybridize and form a double-stranded DNA on the spot carrying probes of complementary sequence. The composition of the bulk solution is deduced from the measured fluorescence intensity of the different spots. Our research [1] concerns the factors determining the performance of DNA chips focusing on probe density and competitive hybridization. In particular, we obtain useful thermodynamics bounds for the performance of DNA chips from their hybridization isotherms. These relate the bulk composition and the hybridization fraction at a given spot in thermodynamic equilibrium. Since both the probes and targets are electrically charged, the hybridization isotherms emerge as Langmuir adsorption isotherms modified to allow for electrostatic interactions in the probe layer: each hybridization event increases the charge of the probe layer thus raising the penalty for the next hybridization event. Two types of competitive hybridization are involved (see Fig. 1): (i) Competitive surface hybridization occurs when two different targets can hybridize with the same probe; (ii) Competitive bulk hybridization arises when the solution contains complementary sequences that hybridize with the targets but not with the probes. The hybridization isotherms allow for the role of competitive hybridization and quantify the resulting reduction in the performance of the chips.

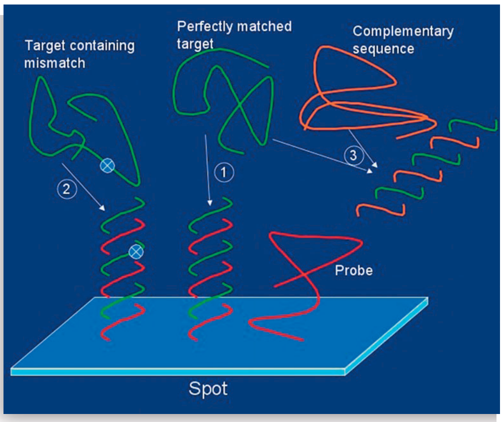

Figure 1: Schematic picture of probes, grafted ssDNA (in red) hybridizing with perfectly matched and mismatched targets in the presence of complementary ssDNA. Competitive surface hybridization involves reactions 1 and 2. Competitive bulk hybridization involves reactions 1 and 3.

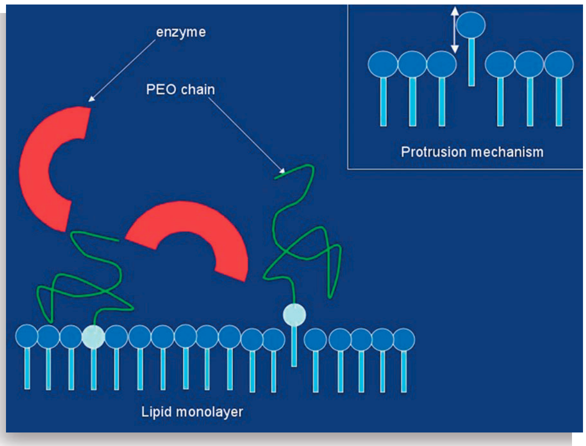

Figure 2: Lipid monolayer incorporating PEO-functionalized lipids. The inset depicts a protruding lipid. The PEO-stabilized protrusions enable the function of interfacial enzymes (in red) to hydrolyze the functionalized lipids.

II. STEALTH LIPOSOME

Stealth liposomes (SL) are vesicles formed by lipid bilayers incorporating two types of lipids: normal lipids and lipids functionalized by short chains of the neutral water-soluble polymer Polyethylene Oxide (PEO) (see Fig. 2). SL are used to deliver anticancer drugs into tumors. The presence of the PEO chains increases the circulation time of the SL in the blood by slowing down their elimination in the liver. The enhanced circulation time is attributed to repression of protein adsorption on the liposomes, an event that triggers their elimination. The repression mechanism of protein adsorption by terminally anchored PEO chains is of interest for a better understanding of SL function. A simple explanation for much of the existing data attributes this function to the osmotic penalty incurred by a protein on entering the PEO layer [2]. For small proteins the penalty is of the form (osmotic pressure in the PEO layer) × (protein volume). It thus allows for the density of the chains and the dimensions of the protein. A new twist to the SL story recently emerged with the discovery that SL are more susceptible than bare liposomes to degradation by interfacial enzymes, secretory phospholipase A_2 (sPLA2), that hydrolyzes lipids incorporated into membranes. This discovery is of interest because sPLA2 are more abundant in cancerous tissue thus affording a mechanism for controlled release of anticancer medication within the tumor. Our work addresses two questions: Why doesn't the PEO repress the activity of the sPLA2? Why does it enhance their function? The answer to the first question is simple. The sPLA2 are small proteins and the osmotic penalty incurred by approaching the membrane is small compared to the thermal energy and thus negligible. The answer to the second question emerges upon realizing that the head group of the lipid must protrude out from the membrane in order to reach the active site of the enzyme [3]. Such protrusions (see Fig. 2) are fluctuations when the lipids are not functionalized. However, protrusions of lipids attached to PEO chains are equilibrium features due to the entropic penalty, arising because the membrane is impenetrable to the PEO chain, which balances the price of exposing the lipid hydrophobic tail.

III. PERSPECTIVE

The two examples discussed above involve polymers whose monomers undergo dynamic equilibrium between two interconverting states ("two-state" polymers). DNA monomers can exist either in a helical or a coil-like state. PEO monomers are thought to interconvert between hydrophilic and hydrophobic states. The "two-state" feature is qualitatively important in the first example and useful for the quantitative analysis of the second. It is present in other water-soluble polymers and can lead to novel configurational and phase transitions of relevance to the design of biomedical devices [4].

[1] A. Halperin, A. Buhot and E. B. Zhulina , Biophys. J. **86,** 718 (2004).
[2] A. Halperin and D. E. Leckband, C.R. Acad. Sci. **1 IV,** 1171 (2000).
[3] A. Halperin and O. Mouritsen, submitted to Eur. Biophys. J.
[4] A. Buhot and A. Halperin, Europhys. Lett. **50,** 756 (2000).

Contact: ahalperin@cea.fr

CELLULAR ADHESION AND CELLULAR MOTILITY*, A PLAYGROUND FOR PHYSICISTS

B. Fourcade[a] **and F. Bruckert**[b]

a: Service des Interfaces et des Matériaux Moléculaires et Macromoléculaires (SI3M), UMR SPrAM 5819, DRFMC
b: Laboratoire Biochimie et Biophysique des Systèmes Intégrés, DRDC, CEA/Grenoble

Investigation of the physical mechanisms of cell adhesion and spreading is just emerging with observations of living cells becoming more and more accurate and rich in information. In the following, we will focus on a working model when a cell adheres and crawls onto a solid substrate.

Les observations et techniques utilisées devenant de plus en plus précises et performantes, la recherche et la compréhension des mécanismes physiques de l'adhésion d'une cellule sont en plein essor. Dans l'article qui suit nous présentons un modèle de travail théorique caractérisant le processus d'adhésion et de décollement d'une cellule vivante sur un support solide.

In the last fifteen years, new experimental and conceptual approaches have increased our knowledge about cellular machinery. Living systems having low contrast from the optical point of view are now commonly observed *in vivo* using interferencial microscopy techniques and fluorescent probes. Moreover, new micro-mechanical devices for single molecule experiments, artificial nano-machines and bio-mimetic systems are constantly invented to probe and model living matter. Cellular machinery has now also become a playground for theory.

We want to understand how and why mechanical and chemical forces work in a very coordinate way at a scale (1μm) where Brownian motion should *a priori* dominate. Cellular biology tells us that the cell is a chemical automaton which responds to an external stress via a cascade of internal chemical and physical reactions. There are fundamental differences between usual self-assembled systems, such as polymers or amphiphiles, and living cells: (i) living matter is out-of-equilibrium; (ii) it is a driven assembly system in the sense that their motion is due to a constant reshaping of the cell structure. The chemistry of this reconstruction is, however, stress-dependent. Thus understanding how forces are distributed and how energy is dissipated may help to understand how the many different biochemical species work together to produce motion.

The simplest method to probe the cell motion properties is to apply a mechanical force on a cell adhering to a solid substrate.

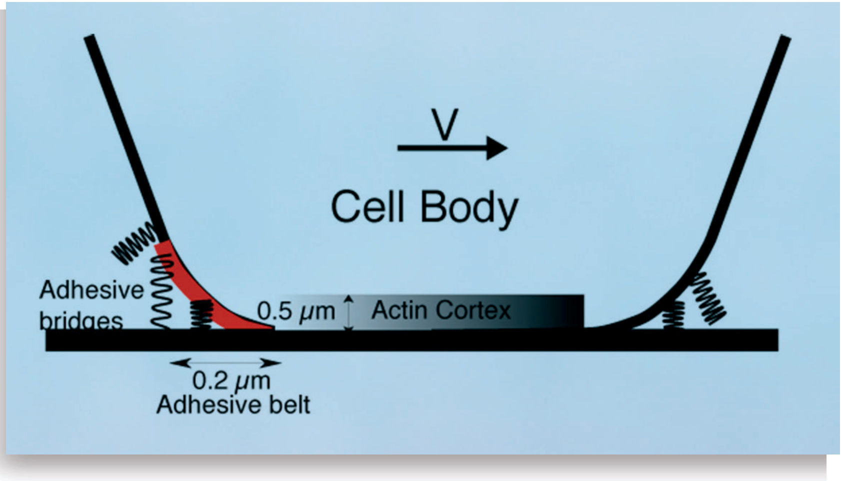

Figure 1: A living cell adhering on a solid substrate is submitted to a steady flow stress. Imaging the cell allows the velocity V of the centre of mass to be measured. Under the action of the external force, the cell crawls and the adhesive bridges are stretched and detached.

---

* motility : mobility and motricity

This can be obtained in a hydrodynamic flux chamber in which water flows parallel to the substrate [1,2]. The cells at the surface seem to move downstream like a passive body. In fact, the backside exposed to the hydrodynamic flux is peeled off the substrate with a constant velocity while the front-side at the opposite face advances by extending protrusions at regular time intervals: actually, the cells are *active* systems. The external hydrodynamic force is not itself the motor of the movement but activates it.

Our schematic model points out the role of the extreme margin of the adhesive zone where the cell is in contact with the substrate (see Fig. 1). This is where the cell "feels" if it has to spread or to peel off. Unlike traditional soft materials for which adhesion occurs via short-range potentials, cellular adhesion occurs because of adhesive bridges. They connect the cell body to the substrate via a complex set of proteins which pierce the membrane and which are anchored into the cell body. This is how adhesive bridges are able to initiate multiple cascades of signals.

Roughly, an adhesive bridge made of proteins has a length of a few tenths of nanometers. The forces of a few pico-newtons which come into play are too small to change the protein structure. From the mechanical point of view, we consider that these proteins are springs with one end anchored on the substrate with a weak interaction such as a hydrogen bond. Thus, the nature of these weak anchoring points is only statistic and thermal fluctuations play an important role. In our picture, peeling the cell off the substrate amounts to disconnecting the adhesive bridges from the substrate. However, as shown in recent single molecule spectroscopy experiments, breaking a non-covalent bond depends on the loading rate and this why the mechanical response of the adhesive belt has remarkable properties.

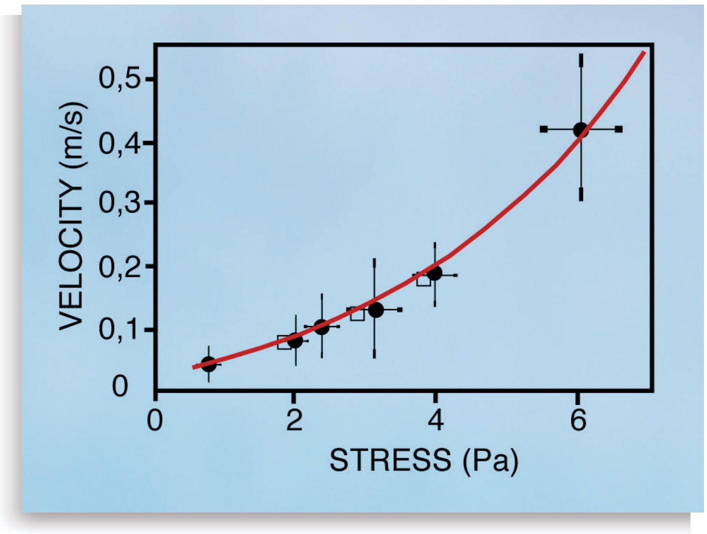

Figure 2: Peeling velocity versus applied stress. The solid curve corresponds to the data adjustment with a theoretical model describing the peeling process.

Because of this very dissipative mechanism, we have shown that the connecting time of the adhesive bridges located at the extreme margin of the cell (the adhesive belt) is the characteristic time for peeling the cell off the substrate. Then the basic task of statistical physics is to model the relationship between the mechanical work applied to the system and the mechanical work necessary to break off the microscopic bonds: to correlate the microscopic to the macroscopic. Both corresponding energies differ drastically, the dissipation being very large. Our model enables the characteristic cell velocity curve versus the applied flow force to be computed.

Figure 2 shows the non-linear increase of the peeling velocity of the cell as a function of the applied force and points correspond to different sets of experimental data. The quasi-exponential behaviour of this curve is the signature of breaking of the adhesive bridges in a thermo-activated regime.

Now our work is geared to understanding how mechanical and chemical forces work together to produce motion and this is where non-equilibrium statistical mechanics comes into play. In our approach, the polymeric network of polymerised actin molecules (actin cortex) at the cell body periphery plays a fundamental role. This network is constantly remodelling itself under the action of the adhesive bridges and this reshaping is the basic process at the origin of the cell movement. The fascinating properties of cell motions is just beginning to be understood from both the biochemical and mechanical points of view. A cell is never at rest. It constantly explores its environment and the role of physics is to help understand the extreme sensitivity of the cellular machine to external signals.

---

[1] E. Decave, D. Garrivier, Y. Brechet, F. Bruckert, and B. Fourcade, Phys. Rev. Lett. **89,** 108101 (2002).
[2] E. Decave, D. Rieu, J. Dalous, S. Fache, Y. Brechet, B. Fourcade, M. Satre, and F. Bruckert, J. Cell. Sci. **116,** 4331 (2003).

Contact: bfourcade@cea.fr

Gd^{3+}-BASED CONTRAST AGENTS IN MAGNETIC RESONANCE IMAGING

P. H. Fries

Service de Chimie Inorganique et Biologique (SCIB), DRFMC

Magnetic Resonance Imaging (MRI) often involves the use of contrast agents. An in-depth characterization at the molecular level of the factors affecting the efficiency of these powerful imaging probes allows their rational design and set-up.

L'Imagerie par Résonance Magnétique (IRM) fait fréquemment appel à l'utilisation d'agents de contraste. La caractérisation approfondie à l'échelle moléculaire des facteurs gouvernant l'efficacité de ces puissantes sondes d'imagerie permet d'optimiser leur conception et leur mise en place.

I. INTRODUCTION

MRI is a powerful and safe technique in diagnostic clinical medicine and biomedical research [1]. The expansion of MRI has prompted the development of new drugs, called contrast agents (CAs). These compounds are administrated to patients in order to target specific parts of the body and locally increase the image contrast (see Fig. 1). Physicians can thus differentiate either normal and diseased tissues or different parts of the body, so as to show organ function or blood flow. About 40% of MRI examinations use CAs and this percentage is increasing with the development of new agents and applications.

MRI is based on nuclear magnetic resonance: In a magnetic field B_0 , an oscillating electromagnetic signal emitted by the nuclear spins I (magnetic moments) of the hydrogen nuclei of water molecules can be measured. The resonance frequency of the signal oscillations is proportional to B_0 . In order to construct an image, a spatial gradient of magnetic field is applied to the living system, leading to a correspondence between the resonance frequency and the spatial position of a voxel (three-dimensional pixel). Computer processing of the total signal emitted by the nuclei of all the voxels makes the image as the spatial juxtaposition of the signals from the various voxels. The signal intensity is proportional to the density of the water molecules in the voxel. Unfortunately, this density parameter cannot give a suitable image contrast in medical MRI since the water densities of the soft tissues in living organisms often have too similar values.

II. LONGITUDINAL RELAXATION CONTRAST AGENTS

To overcome this difficulty, another parameter is used: the longitudinal relaxation rate R_1(r) that represents the speed in s^{-1} at which the components of the nuclear spins I along the field B_0 return to equilibrium after a temporary magnetic perturbation. R_1(r) depends on the physico-chemical nature of the tissue at the spatial position r. Therefore, R_1(r) varies from one voxel to another and gives rise to a position-dependent brightness or contrast. Contrast agents are used for their ability to locally enhance R_1(r). Among the possible paramagnetic metal ions, Gd^{3+} is particularly suitable. Indeed, because of its high electronic spin value $S=7/2$, it has a strong dipolar magnetic interaction H_{dip} with the hydrogen nuclear spins. In addition, Gd^{3+} exhibits a slow electronic relaxation. It can form very stable biocompatible complexes, which are eliminated from the body before release of toxic free Gd^{3+} ions.

The efficiency of a CA depends on the strength and time fluctuations of H_{dip}. These fluctuations are caused by the relative spatial motion of the water hydrogen atoms with respect to Gd^{3+} and by the relaxation of the electronic spin of this ion. We developed various aspects of the molecular mod-

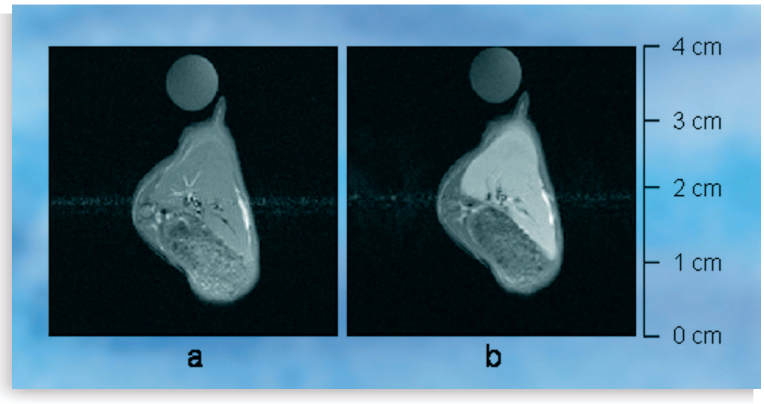

Figure 1: MRI image of a mouse liver. (a): without contrast agent. (b): one minute after injection of a Gd^{3+}*-DTPA derivative (courtesy of S. Boutry, RMN Laboratory of Prof. R. N. Müller, University of Mons, Belgium, EMIL partner).*

eling needed to predict these fluctuations which can be classified according to the fates of representative water molecules as shown in Fig. 2. At an arbitrary time origin $t = 0$, three situations occur. First, water molecules such as wM (1st hydration shell) are directly bound to the metal ion M (grey sphere). Second, other water molecules such as w2S (2nd hydration shell) have a weak H-bond with one of the associating sites (pink) of the CA. Third, the rest of the water molecules such as w1 and w2 (outer-shell situation) undergo a free translational diffusion.

All these molecules are progressively replaced by other water molecules (that do not appear in the figure) initially located in other positions. After 10 ps, the outer-sphere water molecules have already undergone notable displacements while the CA has only rotated by a tiny angle and the 1st and 2nd sphere molecules are still linked to the CA. After 40 ps, the outer-sphere w1 has exchanged with the 2nd sphere w2S. A much longer duration of 1 ns was necessary to observe a 180° rotation of the whole CA. During this period all the water molecules, but wM directly coordinated to Gd^{3+}, have also gone away from the CA. Eventually, after 1 µs, wM has exchanged with a free neighbouring water molecule. All the four previous dynamical mechanisms affect R_1(r), since they occur within periods shorter than the characteristic relaxation time $1/R_1$(r) which is typically in the order of 100 ms to 1 s.

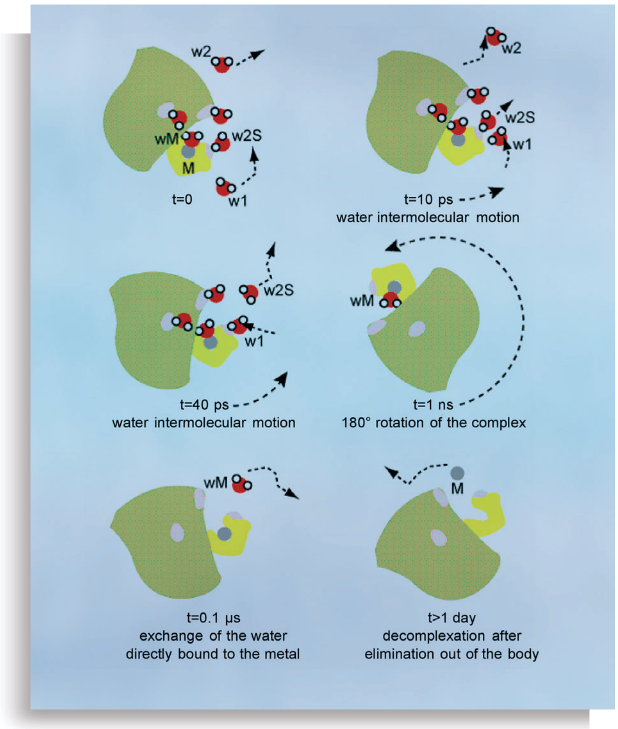

Figure 2: Theoretical description of the fates of typical water molecules which are near a contrast agent at an arbitrary time origin t=0. The ligand (yellow) complexing the Gd^{3+} *ion (grey sphere) is bound to a large biocompatible macromolecule (green).*

III. CONCLUSION

Our contribution to the field of contrast agents [2,3] allows the development of new accurate models and experimental methods that bring insight into the underlying physics. Such studies, which support the rational design of of Gd^{3+} imaging probes, will be pursued in the Network of Excellence EMIL (European Molecular Imaging Laboratories).

ACKNOWLEDGMENTS

This research was carried out in the framework of the EC COST Action D-18 "Lanthanide Chemistry for Diagnosis and Therapy".

[1] P. Caravan, J. J. Ellison, T. J. McMurry, and R. B. Lauffer, Chem. Rev. **99,** 2293 (1999).
[2] P. H. Fries, G. Ferrante, E. Belorizky, and S. Rast, J. Chem. Phys. **119,** 8636 (2003).
[3] E. Belorizky and P. H. Fries, Phys. Chem. Chem. Phys. **6,** 2341 (2004).

Contact: pfries@cea.fr

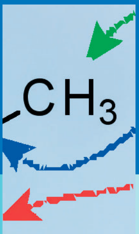

SOME ASPECTS OF DNA BASES STUDIED BY QUANTUM CHEMISTRY TOOLS

A. Grand and F. Jolibois

Service de Chimie Inorganique
et Biologique (SCIB), DRFMC

We have applied a computational protocol to a comprehensive study of the spectroscopic properties of radicals arising from DNA bases. This approach also allowed the description of the pathways involved in their formation as well as calculation of thermodynamic parameters of the reactions.

Nous avons appliqué une démarche théorique pour réaliser une étude approfondie de propriétés spectroscopiques de radicaux issus des bases de l'ADN. Cette approche a aussi permis la description de chemins réactionnels impliqués dans leur formation, ainsi que le calcul de paramètres thermodynamiques de la réaction.

Deleterious effects of ionizing radiation to cells result at least partly from the induction of DNA damage. The large majority of the underlying chemical reactions is triggered by radical species produced upon radiolysis of the water molecules surrounding DNA. Among them, hydroxyl radicals (°OH) and hydrogen atoms (°H) are the most reactive. Elucidation of the pathways leading from the initial water radicals to the final mutagenic and lethal DNA lesions first requires identification of the DNA radicals resulting from the reaction of bases and 2-deoxyribose units with °OH and °H. Subsequently, a more precise description of the sequence of events leading to formation of the latter radical species may be attempted. For both topics, theoretical approaches, based on quantum chemistry tools, provide useful information.

Characterization of DNA base radicals is experimentally mostly achieved by electronic paramagnetic resonance (EPR). Emphasis has been placed on the radical arising from thymine, which is the most reactive base towards °H. The methyl-centered radical (see Fig1) was the first to be identified within irradiated DNA. The two main products of the reaction of thymine with °H, the 5,6-dihydro-6-yl-thymine (hereafter referred to as 6-yl) and 5,6-dihydro-5-yl-thymine (hereafter referred to as 5-yl) radicals were the subject of structural investigations during the past decades. However, this task is not simple because the relationships between EPR spectroscopic parameters and structural features are quite indirect. This led to rather large discrepancies on the results of EPR studies on thymine 5-yl and 6-yl radicals.

In such circumstances, computational approaches are particularly attractive and provide additional information that partly explains these conflicting experimental data. As a matter of fact, the EPR features of the different isomers of the thymine radicals can be calculated precisely [1]. Calculations show that in equilibrium geometries of both 5-yl and 6-yl, the thymine ring is approximately planar with the exception of the carbon atom where hydrogen was added. The latter carbon may be on either side of the average plane of the radical, in so-called half-chair configurations. Inversion of the half-chair is possible for the two isomers. However, energy calculation shows that one form is more stable than the other for 6-yl while both are equally possible for 5-yl (see Fig. 2). In addition, determination of the vibrational wave functions shows that the form with

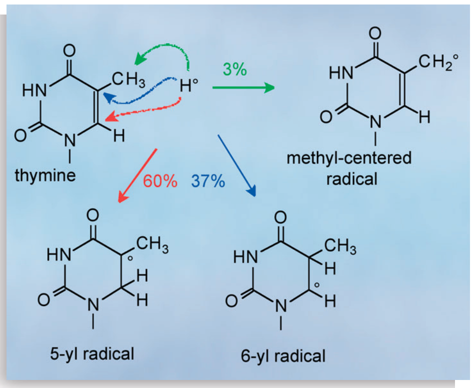

Figure 1: Chemical structure of the radicals arising from the reaction of H° with thymine.

the methyl group in axial position is favored at low temperature for 6-yl. In contrast, constant inter-conversion of one conformation into the other is expected for 5-yl. These calculations also show that, when increasing the temperature and thus favoring higher vibrational levels, variations in the EPR spectra were expected, which actually accounted for some of the scattering in experimental data.

Identification of the geometry of base radicals then enables the sequence of events involved in the addition of °H to the thymine ring to be determined [2]. This description of a chemical reaction cannot be experimentally observed, because intermediates are very short-lived species. Computation thus points out some important features such as the geometry of pre-reactive and transition states. Thermodynamic parameters, including energy and activation barriers, can also be calculated. The main steps of the addition of H° to thymine are displayed in Fig. 3 where each point corresponds to an optimized orientation of the two reagents. The validity of the results is confirmed by the calculated thermodynamic features of the reaction. First, a low value is found for the energy barrier (few kcal/mole) for the formation of both 5-yl and 6-yl radicals, in agreement with the efficiency of addition of H° to thymine. In addition, the enthalpy difference is larger for formation of 5-yl than 6-yl. Moreover, the activation energy of the reaction leading to 5-yl is smaller than for 6-yl. Altogether, these thermodynamic features are in complete agreement with the experimental evidence showing that H° preferentially adds to the C6 position.

The results presented above mainly focused on the addition of °H to thymine. However, the reactivity of hydroxyl radicals °OH, the most reactive product arising from water radiolysis, has also been extensively studied using the same computational approach. Work is also in progress for the other DNA bases [3]. Future investigations will deal with more complicated reactions such as the radical addition between two adjacent DNA bases. The resulting information, combined with the quantification of the final products arising from the initial radical species, will provide insights into the interaction between ionizing radiation and genomic material.

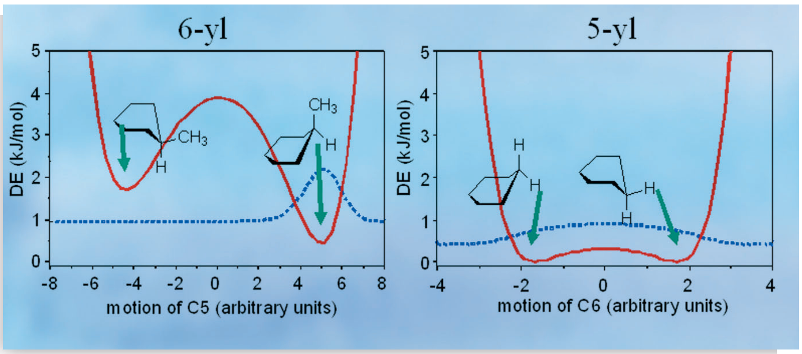

Figure 2: Potential energy (—) and first vibrational wavefunction (- - -) for thymine 6-yl and 5-yl radicals on motion of C5 and C6 atoms, respectively, out of the plane of the molecule. Half-chair structure shown corresponds to conformation in the potential wells.

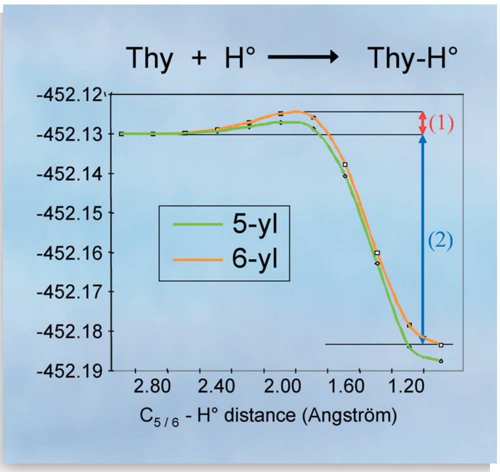

Figure 3: Variation of energy on addition of H° to thymine. The activation energy (1) and enthalpy variation (2) are shown for formation of the 6-yl isomer.

[1] F. Jolibois, J. Cadet, A. Grand, R. Subra, N. Rega, and V. Barone, J. Am. Chem. Soc. **120,** 1864 (1998).
[2] F. Jolibois, A. Grand, J. Cadet, C. Adamo, and V. Barone, Chem. Phys. Lett. **301**, 255 (1999).
[3] C. Adamo, M. Heitzmann, F. Meilleur, A. Grand, J. Cadet, and V. Barone, J. Am. Chem. Soc. **123,** 7113 (2001).

Contact: agrand@cea.fr

HOW TO SEE THE LOCAL STRUCTURE OF A PROTEIN WITHOUT CRYSTALLOGRAPHY

J. M. Mouesca
and S. Gambarelli

Service de Chimie Inorganique
et Biologique (SCIB), DRFMC

By combining quantum-chemical calculations with electron paramagnetic resonance (EPR) measurements, we have built a model linking the local structure of the active sites of [2Fe-2S] proteins to their EPR features. This is a useful tool to characterize these proteins, on the basis of a simple EPR experiment when crystals are not available.

En combinant des calculs de chimie quantique avec des mesures de résonance paramagnétique électronique (RPE), nous avons construit un modèle reliant la structure locale du site actif de protéines [2Fe-2S] aux données de RPE. C'est un outil utile pour caractériser ces protéines, par une simple expérience de RPE, quand des cristaux ne sont pas disponibles.

I. INTRODUCTION

Iron-Sulfur proteins are ubiquitous in the living realm and play fundamental roles in such processes as cellular respiration, photosynthesis, etc. Their active sites contain iron ions linked to sulfur containing groups, for instance in the form of [2Fe-2S] clusters (see Inset1) (see Fig. 1a). The geometry of the active site appears to be a key parameter in the reactivity of the protein. X-ray crystallography is the choice method to obtain the 3D structures. Unfortunately, in the case of [2Fe-2S] proteins, only a handful of proteins have been crystallized and characterized among the hundreds isolated. In contrast, these systems are easily characterized by electron paramagnetic resonance spectroscopy (EPR) (see Inset2) which requires very small amounts of biological products. However, the basic quantity derived from EPR, the g-tensor (Fig. 1b), is difficult to correlate to the cluster electronic structures. A *phenomenological* model of the [2Fe-2S] g-tensor published in the late 1970s (B-G model) [1] was based on a wrong geometry because structural data were not available at that time.

Our strategy [2] to link EPR data to geometric features consisted firstly in finding which structural feature is responsible for the variation of the g tensors, and secondly in constructing a subsequent model which allows for computation of the g-tensors. We finally confronted our predictions with known experimental data.

1. [2Fe-2S] ferredoxins

[2Fe-2S] ferredoxins are small electron-transfer proteins found in bacteria, plants and animals. These proteins are folded chains of amino-acids embedding a [2Fe-2S](Cysteine)$_4$ cluster, close to the protein surface, whose iron atoms are linked to the main proteic skeleton via two cysteines each. The paramagnetic EPR-active state is made of one ferrous and one ferric ion.

2. EPR & g-tensors

Electronic Paramagnetic Resonance (EPR) is a spectroscopic technique analogous to Nuclear Magnetic Resonance (NMR). In both methods, spins are submitted to a static magnetic field H and interact with electromagnetic radiations of energy hν. Each spin system resonates at a specific field value, and is thus characterized by a quantity called the g-factor for electronic spins (EPR, via $h\nu = g\mu_B H$, where μ_B is the Bohr magneton) or the *chemical shift* for nuclear spins (NMR). In complex systems, because of the anisotropy, the g-factor is changed into a g-tensor, characterized by three eigenvalues g_1, g_2 and g_3, which depend on the nature of the molecular orbitals involved and on their relative energies.

3. Density Functional Theory

The Density Functional Theory (DFT) is an *ab initio* quantum chemistry method where the fundamental quantity is the electron density. The DFT is particularly well suited for computation of the electronic structure of polymetallic clusters, in which the localized metal spins are magnetically coupled via the exchange interaction.

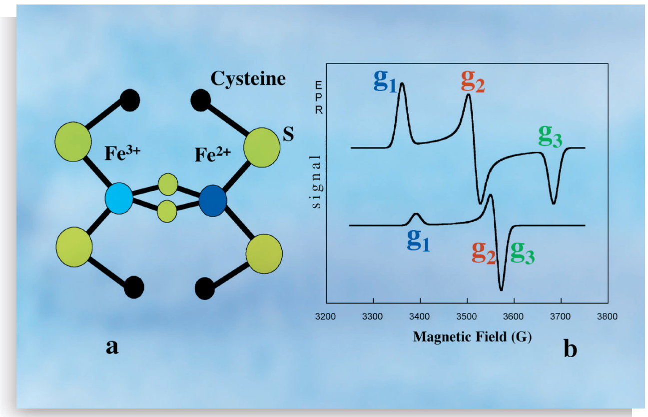

Figure 1: (a): Schematic representation of a [2Fe-2S] cluster. (b): Typical rhombic (top) and axial (bottom) [2Fe-2S] cluster EPR spectra. The three g-values are linked to the field through the relation $g = h\nu / (\mu_B H) = 6883 / H(G)$.

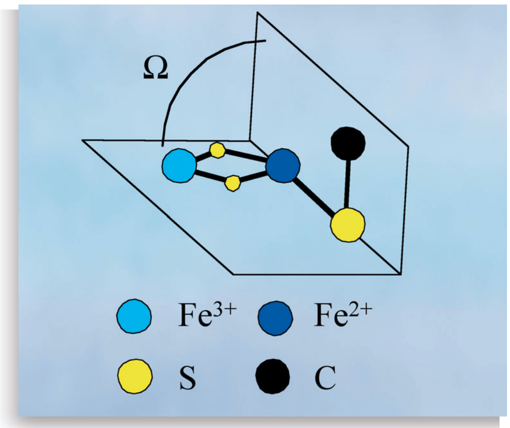

Figure 2: Visualization of the planes defining a Fe-Fe-S-Cysteine-dihedral angle in a [2Fe-2S] cluster.

II. THEORETICAL MODEL

We suspected that the main parameter influencing the g-tensor was the orientation of the sulfur lone pairs of the cysteine amino-acid ligands, acting on the energies of the iron d orbitals. Consequently, we first listed the available 3D structures of the known [2Fe-2S] proteins. We looked at the orientations of the cysteines relative to the cluster, determining the position of the sulfur lone pairs, and selected the relevant structural feature: the Fe-Fe-S-Cysteine dihedral angles.

In each protein, we observed that the two dihedral angles on the ferrous (Fe^{2+}) site were nearly identical, the average angle Ω varying between 120° and 150° (see Fig. 2). We quantum-mechanically computed the g-tensors, by DFT (see Inset3), for a simplified molecular model: [2Fe-2S](SH)4, replacing the four cysteines by SH ligands, and varying Ω from 0° to 180° (see Fig. 3a).

We finally confronted our theoretical results with experimental data by plotting the g-tensors as a function of Ω for the few systems for which both EPR and X-ray data are available (see Fig. 3b). The agreement is qualitatively (rhombic g-tensors for Ω=120°, axial ones for Ω=150°) and quantitatively good.

III. CONCLUSION

For the first time, it has been possible to link the variation of the [2Fe-2S] g-tensors to a specific structural parameter. With such a tool, the biologists' community can now appreciate through a simple EPR experiment the local geometrical environment of the [2Fe-2S] active sites, which also affects the redox potential, the electron transfer rate, the network of hydrogen bonds, etc. This has been a challenge from a computational point of view, but our new model enables the spectroscopists' community to interpret a whole set of spectroscopic observables (EPR, Mössbauer) in a coherent fashion.

We finally open the way for correlation between "simple" spectroscopic data and precise geometrical features in the world of Iron-Sulfur proteins, of which interesting functions are continuously being discovered [3] (various hydrogenases, nitrogenases…).

ACKNOWLEDGMENTS

We thank J. Meyer and M. Fontecave (DRDC, CEA/Grenoble), and J. C. Fontecilla (IBS/Grenoble) for their interest and helpful discussions.

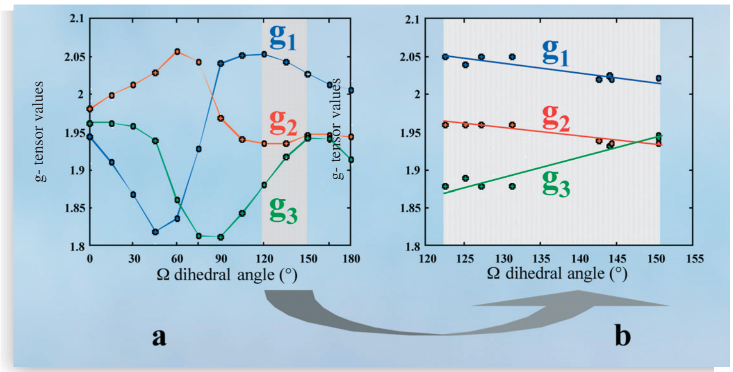

Figure 3: (a): Theoretical (DFT) variations of the three g values as a function of Ω. The grey zone corresponds to the Ω range observed in actual proteins. (b): Plot of the three experimental g values as a function of Ω for known proteins. In the latter scheme, trends in the variation of the g values are outlined by regression lines.

[1] P. Bertrand and J.-P. Gayda, Biochim. Biophys. Acta **579,** 107 (1979).
[2] S. Gambarelli and J.-M. Mouesca, Inorg. Chem. **43,** 1441 (2004).
[3] See for instance "Iron-Sulfur proteins" in *Adv. Inorganic Chemistry* Vol. 47, edited by A. G. Sykes and R. Cammack (Academic Press, London, 1999).

Contact: jmouesca@cea.fr

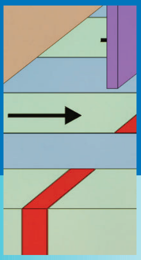

MULTI-TRACK READING HEADS

**L. D. Buda, J. Ch. Toussaint,
I. Firastrau, and J.-P. Nozières**

Service de Spintronique et Technologie
des Composants (SPINTEC), URA 2512,
DRFMC

Nowadays, the size of magneto-resistive reading heads has reached the micron range. The magnetic behavior of such confined systems can no longer be described by macroscopic models. So, we have developed an original approach, able to deal simultaneously with magnetic systems of very different sizes, one macroscopic and the other microscopic.

Aujourd'hui, les dimensions des têtes de lecture magnéto-résistives ont atteint le domaine du micron. Leur réponse magnétique ne peut plus être décrite par des modèles macroscopiques. Aussi, avons nous développé une approche originale, capable de traiter le couplage entre des systèmes magnétiques de tailles très différentes, l'un macroscopique et l'autre microscopique.

The design of advanced magnetoresistive (MR) reading heads requires a deep understanding of the fine interactions between the sensor micromagnetics, the media magnetic pattern and the magnetic behavior of macroscopic elements such as the magnetic shields (see Fig. 1). In a reading head the active element (the sensor) is inserted between two magnetic shields which serve the purpose of concentrating the field produced by the media. There is a large scale difference between all these elements. The shields and media are of micron size or larger, while the sensor has dimensions comparable with the characteristic lengths of magnetic materials (exchange length and magnetic domain wall width) which are in the order of the nanometer. Modeling of such systems therefore involves a complex computational issue since some elements of the head have to be treated macroscopically while the active element has to be analyzed at nanometric scale by a micromagnetic approach [1].

Up to now, the magnetic field generated by the media is usually calculated by bi-dimensional models limited to ideal shields having infinite permeability (without stray field). For three-dimensional heads with arbitrary permeability, large scale Finite Element Method (FEM) computation could be used. Because the MR reading heads for disk/tape drives discussed here are systems with very different characteristic length scales, we preferred to use the Boundary Element Method (BEM) since, for continuous and linear media, only the surfaces/interfaces are discretized and not the whole volume as in a common FEM approach: this therefore saves a lot of computation time.

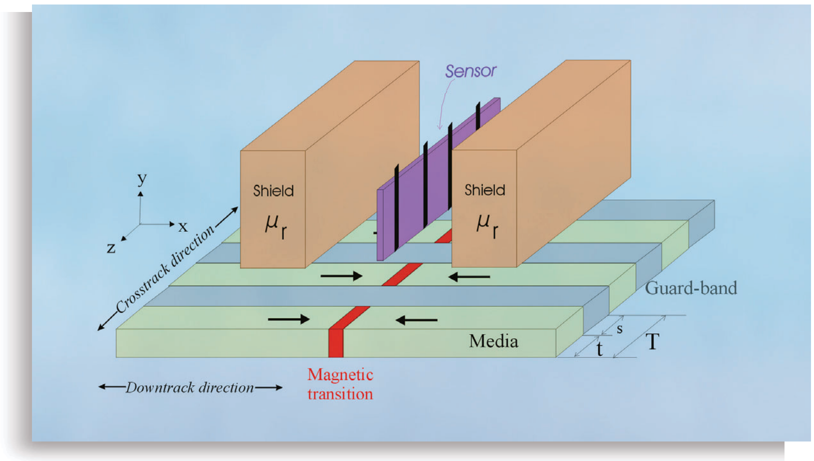

Figure 1: A shielded multi-track magnetic reading head (sensor and shields) flying above a longitudinal media. During the reading process, the head moves along the downtrack direction and reads information stored along the crosstrack direction.

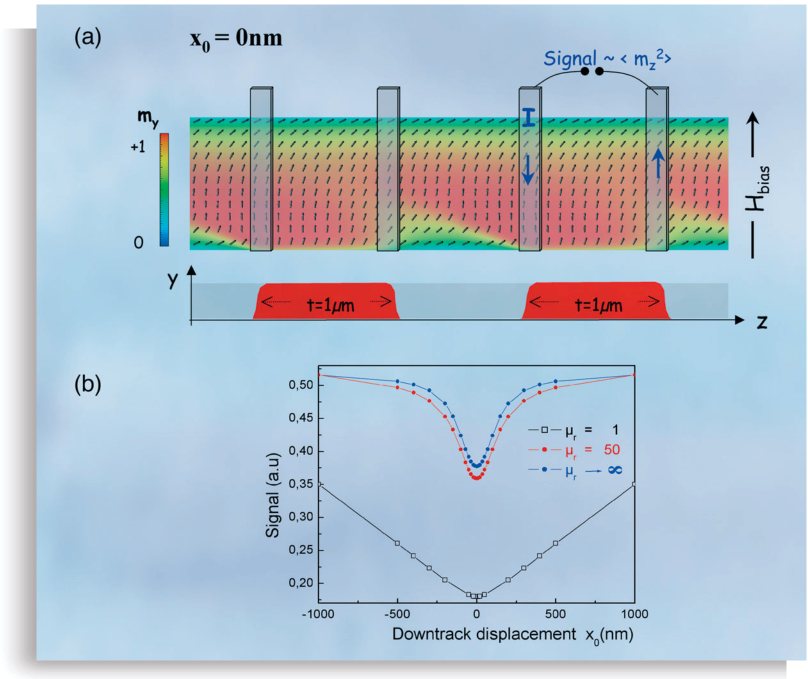

Figure 2: (a): Magnetic stable state of a magnetoresistive head. The head is centered exactly above the magnetic transitions and the magnetization distribution is plotted in the yOz plane. The magnetic volume charges of the transitions ($t = s = 1\mu m$) are drawn below along the crosstrack direction Oz. (b): Simulation of the read transfer curve of the head for shields with various magnetic permeabilities.

In the case of longitudinal magnetic recording, the magnetization lies in the plane of the thin media, and the information is stored by the presence (bit 1) or absence (bit 0) of a magnetic transition (see Fig. 1). The thin active element of the reading head picks up the magnetic field generated by magnetic transition written on the media. To evaluate this field in the presence of macroscopic shields characterized by a finite magnetic permeability µr, the Poisson's equation for the scalar magnetic potential is solved. In addition, for multi-track data patterns as encountered in tape drives, the magnetic scalar potential may be estimated with a good approximation by considering a periodic system along the crosstrack direction (Oz). By applying the Fourier series expansion for the magnetic charge distribution along the crosstrack direction, the initial BEM three-dimensional problem can be treated as a bi-dimensional problem. In fact, the magnetic scalar potential is now the solution of a modified Helmholtz type equation. The method is conceptually straightforward, but some care had to be taken in order to ensure numerical accuracy.

The spatial distribution of the magnetostatic field evaluated by BEM serves as an input to a classical micromagnetic description of the sensor response. Briefly, the magnetic state of the sensor is the result of competition between several interactions: the exchange interaction, the magnetocrystalline anisotropy, the magnetostatic interaction and Zeemann coupling. Each possible magnetic stable state corresponds to a local minimum of the total free energy. These equilibrium states may be reached by integrating the Landau-Lifshitz-Gilbert equation [2] which governs the dynamics of magnetization. For a crosstrack data pattern consisting of alternating transitions and guard-bands schematically drawn in Fig. 1, the magnetization distribution of the MR sensor, as predicted by micromagnetic simulation, is depicted in Fig. 2a. The distribution of the magnetization is directly linked to the electrical response of the sensor. Supposing that the head moves along the downtrack direction, the read transfer curve may be reconstructed (see Fig. 2b) and then compared with experimental data.

Thus by coupling the Boundary Element Method and the micromagnetic approach, we fully describe the behavior of the magnetic sensor in its environment. Problems such as cross-talks between adjacent tracks could be addressed. This numerical approach is a useful tool to design optimized multi-track magnetoresistive reading heads.

---

[1] I. Firastrau, L. D. Buda, J.-Ch. Toussaint, and J.-P. Nozières, J. Magn. Mater. **272-276,** 738 (2004).
[2] O. Fruchard, J.-P. Nozières, B. Kevorkian, J.-C. Toussaint, D. Givord, F. Rousseaux, D. Decanini, and F. Carcenac, Phys. Rev. B **57,** 2596 (1998).

Contact: lbuda@cea.fr

ELECTRON TRANSPORT PERPENDICULAR TO THE INTERFACES IN MAGNETIC MULTILAYERS

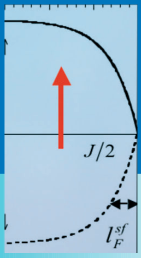

B. Dieny[a], **A. Vedyaev**[b] **and N. Strelkov**[b]

a: Service de Spintronique et Technologie des Composants (SPINTEC), URA 2512, DRFMC
b: Lomonosov State University, Moscow

When an electrical field is applied perpendicular to the interfaces of a magnetic metallic multilayer, the drift of the conduction electrons is spin-dependent and varies from layer to layer. These variations result in local spin accumulations which are counterbalanced by spin relaxation effects.

Quand un champ électrique est appliqué perpendiculairement aux interfaces d'une multicouche métallique magnétique, le mouvement de dérive des électrons dépend du spin et varie d'une couche à l'autre. Ces variations conduisent à des accumulations locales de spin contrebalancées par des effets de relaxation de spin.

The discovery of giant magneto-resistance in (Fe/Cr) multilayers in 1988 launched very intense activity on spin-dependent transport in magnetic multilayers. The invention of spin-valves [1] which exhibit giant magneto-resistance at low fields had a tremendous impact on magnetic recording technology. Indeed these materials are nowadays used as sensing element in read heads of computer disk drives. A metallic magnetic multilayer consists of a stack of magnetic layers separated by a non magnetic spacer layer. The materials are chosen so that the relative orientation of the magnetization in the successive layers can be varied by application of an external field. As the relative orientation changes from parallel to anti-parallel, the multilayer varies from low to high resistance. Information is retrieved from recorded bits by monitoring the multilayer resistance as the read head goes through the magnetic fields they create.

In metallic magnetic materials, the electron transport properties depend on the relative orientation of the electron spin with respect to the local magnetization. For instance in Co, the conductivity of the electrons with spin parallel to the local magnetization is six times larger than for electrons with antiparallel spin. As a result, the net current is spin polarized parallel to the magnetization. Let us then consider an interface separating two magnetic layers of opposite magnetization (see Fig.1) and assume that a current is flowing from right to left i.e. electrons are drifting from left to right. In the left ferromagnetic layer, far from the interface, the current is mainly carried by spin ↑ electrons. The spin ↑ current is given by

$$j^{\uparrow} = \frac{J}{2}(1+\beta)$$

where J is the total current density and β is a characteristic scattering asymmetry parameter (about 0.7 in Co). The spin ↓ electrons carry a smaller current

$$j^{\downarrow} = \frac{J}{2}(1-\beta).$$

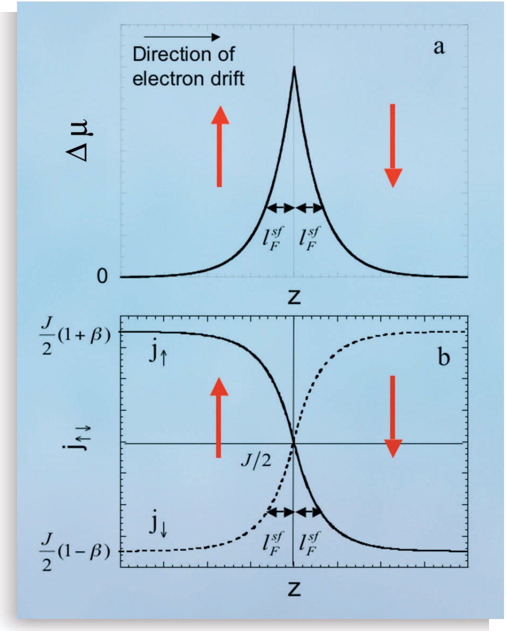

Figure 1: Illustration of spin accumulation at a single interface separating two ferromagnetic layers of opposite magnetization. The large arrows represent magnetization orientation. (a): Spatial variation of the difference in chemical potential $\Delta\mu = \mu^{\uparrow} - \mu^{\downarrow}$ *between the two species of electrons:* $\Delta\mu > 0$ *means an accumulation of spin ↑ electrons at the interface. (b): Spatial variation in current density for each spin channel (adapted from [2]).*

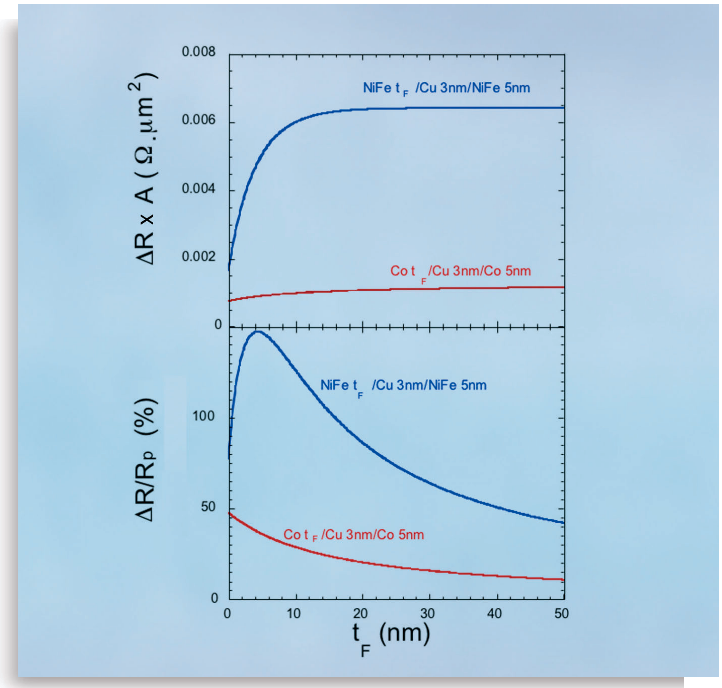

Figure 2 : Example of calculation of magneto-resistance of NiFe t_F/Cu 3nm/NiFe 5nm and Co t_F/Cu 3nm/Co 5nm sandwiches versus thickness of one of the ferromagnetic layers. Absolute magneto-resistance × area product and relative MR ratio.

On the right-hand side, the magnetization is down and the roles of spin ↑ and spin ↓ electrons are inverted. More spin ↓ electrons flow away from the interface than spin ↑ electrons. Within each spin channel, there is therefore an unbalance between the number of electrons moving towards and away from the interface per unit time. This results in a spin accumulation which consists of a local excess of spin ↑ electrons around the interface and a correlated local deficit in spin ↓ electrons. In steady state, this spin accumulation is counterbalanced by spin flip processes (spin orbit interaction and magnon scattering). The characteristic length scale over which the electrons maintain their spin orientation in a given material is the spin diffusion length l^{sf}. The balance between the spin accumulation and spin relaxation leads to local variations in the difference Δμ of electrochemical potential of spin ↑ and spin ↓ electrons as illustrated in Fig.1. The result is a small non equilibrium local magnetization near the interface, proportional to the current.

The Valet and Fert theory [2] addresses the effect of spin accumulation, using a macroscopic model based on two basic equations. A first equation describes spin relaxation effects whereas the second is a spin-dependent generalized form of Ohm's law. By solving these equations within each layer and connecting them from layer to layer by a transfer matrix technique, we have developed a numerical code which enables the resistance and magneto-resistance of any magnetic multilayered stack to be calculated, taking spin-flip processes into account [3]. This code is currently being used by head manufacturers for optimization of spin-valve stacks with current flowing perpendicularly to the interfaces. This approach allows a much faster optimization of the stack composition. We have studied sandwich structures of the form NiFe t_F /Cu 3nm/NiFe 5nm and Co t_F /Cu 3nm/Co 5nm versus thickness of one of the ferromagnetic layers. Figure 2 shows a comparison of the variation of the magneto-resistance expressed both in terms of absolute change in resistance times area (ΔR×A) and relative change of resistance between parallel and antiparallel magnetic configurations. The main differences between NiFe and Co are their resistivities (25μΩ.cm for NiFe and 15μΩ.cm for Co) and their spin diffusion length (l^{sf}_{NiFe}= 4.5 *nm* and l^{sf}_{Co} =15 *nm*). The larger NiFe resistivity is at the origin of the larger magnetoresistance amplitude observed in the NiFe based structures. It also emphasizes the role of bulk scattering with respect to interfacial scattering leading to the presence of a maximum in ΔR/R not observed with Co. In head applications, ΔR is related to the amplitude of the signal whereas ΔR/R relates to the signal to noise ratio. According to Fig. 2, NiFe layers with thickness about 4nm would optimize the transport properties of the device.

The semi-classical theory of spin-dependent transport perpendicular to the interfaces in magnetic metallic multilayers was generalized to calculate the resistance and magneto-resistance from the knowledge of the transport properties of the material constituting each layer. This approach is used for optimization of structures implemented in magneto-resistive heads. ▮

---

[1] B. Dieny, V. S. Speriosu, S. Metin, S. S. P. Parkin, B. A. Gurney, P. Baumgart, and D. Wilhoit, Appl. Phys. **69,** 4774 (1991).
[2] T. Valet and A. Fert, Phys. Rev. B **48,** 7099 (1993).
[3] N. Strelkov and A.Vedyaev, Journ. Appl. Phys. **94,** 3278 (2003).

Contact: bdieny@cea.fr

BOILING CRISIS: THEORY, SIMULATION, AND EXPERIMENTS

V. Nikolayev and D. Beysens

Service des Basses Températures
(SBT), DRFMC

Boiling is a very efficient way to transfer heat from a heater to the liquid heat carrier. We discuss the boiling crisis, a sharp decrease in the heat transfer rate, which can cause a major accident in industrial heat exchangers. Numerical simulation of the growth of vapor bubbles has been found to be in very good agreement with experimentally observed results.

L'ébullition est un moyen très efficace de transférer la chaleur d'un élément chauffant à un liquide caloporteur. Nous discutons la crise d'ébullition, une chute brutale du transfert de chaleur, susceptible de causer un accident grave dans des échangeurs de chaleur industriels. La simulation numérique de la croissance des bulles de vapeur s'est révélée en excellent accord avec des résultats observés expérimentalement.

Boiling is observed commonly in everyday life. This is why it seems well understood. It is true that boiling has been extensively studied from an empirical point of view for the most common fluids and regimes, for instance for water at atmospheric pressure and moderate heat flux supplied to fluid. However, the basic theory of boiling remains *terra incognita*. These difficulties originate from the violence of the fluid motion that on the one hand conceals the mechanisms of bubble growth from detailed observation, and on the other hand hugely complicates direct numerical simulations. Most still unanswered questions concern the close vicinity of the heating surface, down to the scale of bubbles growing at the surface of the heater especially during boiling at high heat fluxes common for industrial heat exchangers, e.g. nuclear power plant steam generators.

Two main boiling regimes can be distinguished: nucleate boiling and film boiling. The former can be commonly observed in a sauce pan. It features separate vapor bubbles that nucleate (i.e. form) and grow at the heater. This regime provides a very efficient heater-liquid heat exchange due to their direct contact. The other regime features a vapor film that separates the liquid from the heater. Film boiling can be also observed in the kitchen by sprinkling water onto a hot frying pan. In spite of the large temperature of the heater (the pan) the water drops survive for a long time precisely due to the thermally insulating vapor film that prevents the liquid from touching the pan. Obviously, the heater-liquid heat transfer is much lower than in the first case.

The subject of our study is the transition from nucleate to film boiling which is called "boiling crisis". During this transition, separate bubbles at the heater are replaced rapidly by a continuous vapor film. This blocks the heater-liquid heat transfer and thus leads to a rapid increase of the heater temperature. If the power is not switched off immediately, the heater can melt down which can cause a major accident if an industrial installation is involved. The boiling crisis occurs at a critical value of the heating flux (fortunately not attainable under "kitchen" conditions).

In spite of its importance, the mechanism of the boiling crisis remains poorly studied. Our purpose is to explain why, how, and when the vapor film begins to form. We have made the fundamental hypothesis that the boiling crisis is triggered by the vapor recoil when liquid transforms into vapor.

Every fluid molecule evaporated from the liquid interface causes a recoil force analogous to that created by the gas emitted by a rocket engine. It pushes the interface towards the liquid side in the normal direction. This force appears because the fluid necessarily expands while transforming from liquid to gas phase. Obviously, the stronger the evaporation rate, the larger the vapor recoil force.

Let us now consider the variation of the evaporation rate along the surface of a bubble growing at the heating surface. Since the fluid is hotter close to the heater than far from it, the evaporation distributed along the bubble surface is strongest in the vicinity of the line of contact of the bubble surface with the

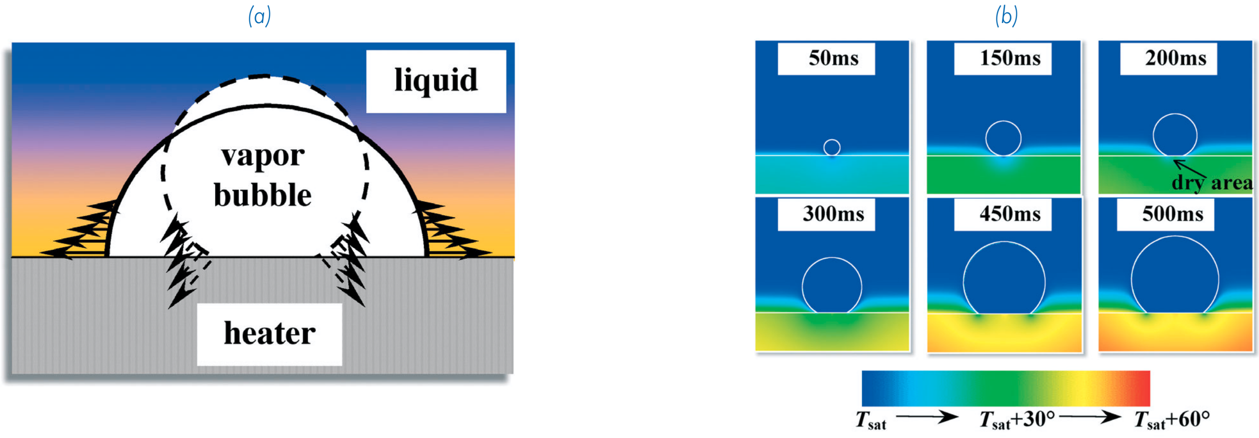

Figure 1. Vapor bubble spreading under the influence of vapor recoil.
(a): Sketch illustrating the vapor recoil effect. The amplitude and direction of the vapor recoil force are shown by arrows.
(b): Simulation results. The color indicates the local temperature with respect to the saturation temperature T_{sat}.

heater. The vapor recoil is also strongest at the contact line and therefore tends to pull the contact line outward, thus spreading the dry area or "dry spot" under the bubble (see Fig. 1a).

A numerical simulation [1] of such a process is presented in Fig. 1b. Such a simulation requires solving of extremely delicate thermal and capillary problems. It can be seen that the dry spot is initially very small and remains so during the initial growth stage. At about 180ms the dry spot begins to grow suddenly, i.e. the bubble spreads. Such a spreading represents the beginning of formation of the vapor film characteristic for the boiling crisis. Figure 1b also shows formation of a hot spot at the heater surface in the middle of the dry area. This temperature rise illustrates the already discussed blocking of the heat transfer by vapor.

This theoretical approach can be compared to an experiment [2] carried out with SF_6 fluid near its critical liquid-gas point. This experiment takes advantage of so-called "critical slowing down" of the bubble growth observed near the critical point. In fact, the growing process of a single vapor bubble could be observed during 45 min thus allowing for a very detailed analysis. The choice of SF_6 was made for practical reasons: the critical point of this fluid is at 45.6°C, 38 bar and requires much less severe conditions for the experiment than for example water (374°C, 220 bar). However, near-critical bubble growth experiments have an important drawback. Since the surface tension becomes very low near the critical point, gravity completely flattens the liquid interface. Weightlessness conditions are thus necessary to preserve the usual convex bubble shape. Some of the results of this experiment performed on board the Mir space station are presented in Fig. 2a. The sequential photos of the growing vapor bubble were taken through the transparent bases of the cylindrical cell, the lateral copper walls of which are being heated. Spreading of the dry spot under the bubble similar to that in Fig. 1b can be seen. The bubble shapes calculated for different values of the vapor recoil strength *N* are presented for comparison in Fig. 2b. The correspondence is striking.

Generally speaking, the comparison between the results presented above shows the complementarity of theory (basic assumptions), experiment (test of the validity of a model) and simulation (access to parameters not attainable by experiments).

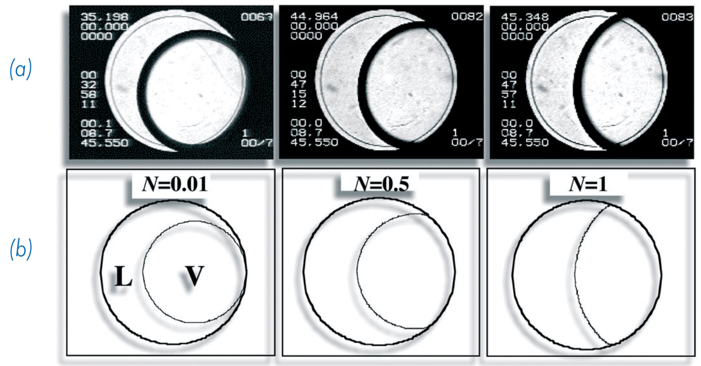

Figure 2. Snapshots of the vapor bubble (V) growing in near critical liquid (L), both experimental (a) and calculated (b) for the given values of the vapor recoil strength N.

---

[1] V. S. Nikolayev, D. Beysens, G.-L. Lagier, and J. Hegseth, Int. J. Heat Mass Transfer **44,** 3499 (2001).

[2] Y. Garrabos, C. Lecoutre-Chabot, J. Hegseth, V. S. Nikolayev, D. Beysens, and J.-P. Delville, Phys. Rev. E **64,** 051602 (2001).

Contact: vnikolayev@cea.fr

PULSE TUBE CRYOCOOLERS

J. M. Poncet and R. Vallcorba

Service des Basses Températures (SBT), DRFMC

There is a growing demand for small cryocoolers due to the emergence of specific applications requiring low-temperature operation, typically in the 80 K to 4 K range. Pulse tube refrigerators are very promising in this regard. We report on efforts made in our laboratory to develop a calculation model for this device.

Il y a une demande croissante pour des petits cryoréfrigérateurs qui est due à l'apparition d'applications spécifiques fonctionnant à basse température, typiquement dans la gamme de 80 K à 4 K. Les réfrigérateurs à tube pulsé sont très prometteurs à cet égard. Nous évoquons les efforts faits dans notre laboratoire pour développer un modèle de calcul pour cet appareil.

The need for small cryocoolers arises in different fields of activity. For example, electromagnetic radiation detectors (infrared to x-ray) used in astronomical and earth observation require cooling well below room temperature for better sensitivity. Devices containing superconducting components need refrigeration below characteristic critical temperatures (typically between 50 and 80 K). Basic research on material properties is often performed at low temperatures. In all these applications, the purpose of the cryocooler is to cool objects and to maintain them at a specified operating temperature by absorbing the heat released from these objects and from their immediate environment (thermal conduction through mechanical structures, thermal radiation from surrounding hot surfaces ...).

In most types of cryocoolers, periodic gas expansion is used to produce the refrigeration effect [1]. A working gas (helium) follows a closed thermodynamic cycle. Expansion and heat absorption take place at a special section - the cold source. Compression associated with heat release is usually performed at room temperature (hot source). Pulse tube cryocoolers make use of pressure waves. The basic principle is shown on the left-hand side of Fig. 1: a compressor unit (pressure oscillator) generates a pressure wave which propagates through a set of two tubes, the regenerator and the pulse tube, before reaching the subsystem labelled impedance.

The regenerator tube is filled with porous material and, in stationary operation, exhibits a temperature gradient span-

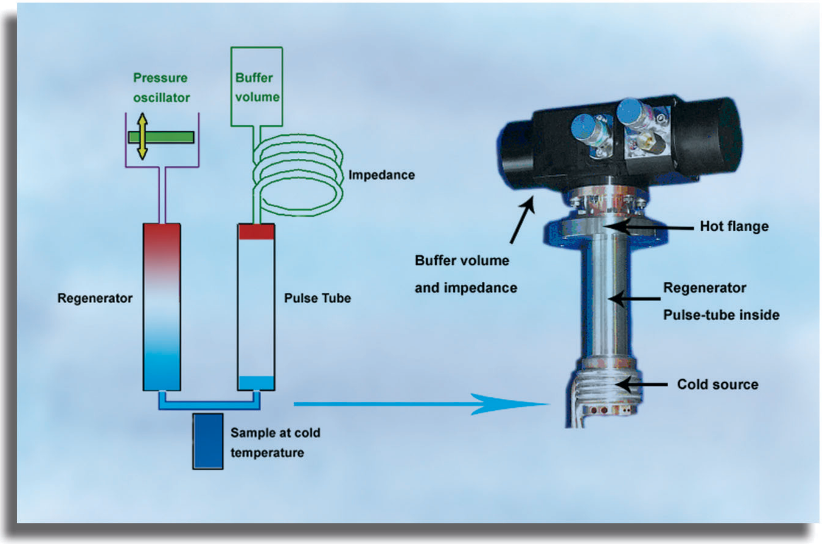

Figure 1: Pulse tube cryocooler. Left: schematic, colours roughly indicate temperature distribution, red – hot, blue – cold. Right : Practical example for medical applications. The regenerator and pulse tube are in a concentric configuration; only the regenerator is visible. The device is used to cool a superconducting antenna.

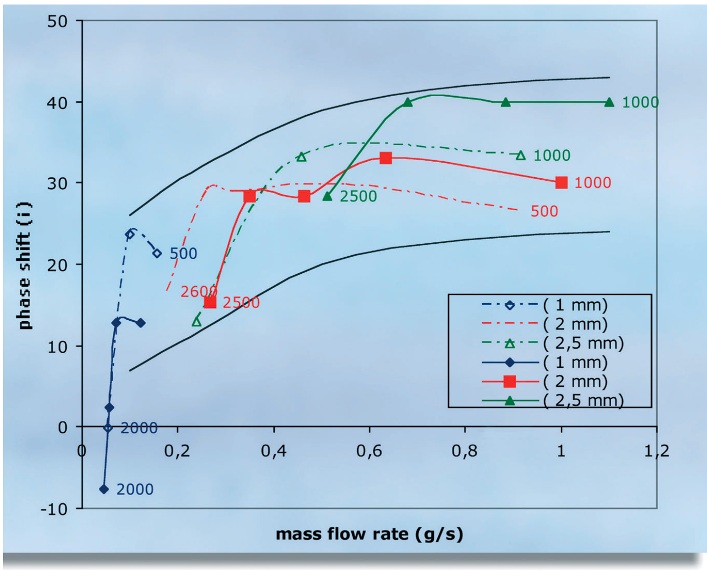

Figure 2 : Phase shift vs. flow rate for different geometries of the capillary in the impedance device. The diameter of the capillary is indicated by the colour, its length in mm is marked on the curves. (solid line – numerical results), (dashed line – experimental results).

ning the gap between the cold source and room temperature. Its function is to cool down the incoming helium gas on its way to the cold source. It acts like a thermal sponge by alternately absorbing heat from the incoming gas and releasing heat to the outgoing gas. The pulse tube is nothing more than an empty thin-walled tube entirely filled with the working gas which behaves somewhat like a virtual piston. The phase shift between the oscillating gas flow and the pressure wave is the key parameter which governs the cooling effect at the cold end. For optimum performance, it should be nearly zero at that location. The special impedance device (here a capillary associated with a buffer volume) connected to the hot end of the pulse tube allows correct adjustment of this parameter. The phase shift at the hot end is related to that at the cold end via the flow impedance of the pulse tube.

The major advantages over other types of cryocoolers (Stirling, Gifford-MacMahon) are the lack of moving parts at the cold source and the associated reduction of vibration. The consequences are excellent reliability and simplified fabrication. A practical example of a compact pulse tube cryocooler for medical application is shown on the right-hand side of Fig. 1.

The two main features of cryocooler performance are cooling capacity and thermodynamic efficiency. In the pulse tube cryocooler, these features are mainly determined by the regenerator efficiency and the pressure/flow phase shift along the pulse tube. Many parameters come into play: the properties of the regenerator material (specific heat, thermal conductivity and diffusivity), the size of the pulse and regenerator tubes, the characteristics of the impedance device and of the pressure wave generator. Their number is too large and their influence too complex to allow a performance prediction based on simple empirical scaling laws.

This apparently simple technological object is therefore an open study subject for theory. As part of an ongoing development programme in our laboratory, long-standing efforts have been made to establish calculation models for pulse tube operation as a tool for performance prediction and, more generally, for design of advanced prototypes.

Two types of models have been developed: global models which concern the operation of the entire cooler [2] and sector models which describe one of the relevant components in detail. Our first global model was based on analytic algorithms and allows fast calculation of a large number of geometrical configurations. The assumptions and simplifications made in this model (ideal gas properties for helium, simplified regenerator) do however limit its application to cycles with cold source temperatures above 15 K.

A second global model was recently completed. It includes a real gas state equation for helium and uses numerical methods for the regenerator operation. After full validation it will be suitable for temperatures down to the 4 K range.

A sector model has been developed for the impedance device. It focuses on the study of the phase shift effect created by a capillary and a buffer volume. Figure 2 shows a comparison between calculated and experimental results [3] which, among other things, reveal forbidden zones in the flow rate/phase shift plane. In the diagram, these zones clearly appear outside black boundary lines. For example, a phase shift of 40° can only be obtained with mass flow rates larger than 0.6 g/s.

ACKNOWLEDGEMENTS

We wish to thank our colleagues P. Seyfert and I. Charles for helpful discussions.

---

[1] L. Duband and A. Ravex in *Handbook of Cryogenics Engineering*, edited by J. G. Weisend II (Taylor&Francis, Philadelphia/USA, 1998) p.287.

[2] A. Ravex, P. Bleuzé *et al.*, 19th International Congress of Refrigeration, proceedings IIIb, (International Institute of Refrigeration, Paris/France, 1995) p.1209.

[3] I. Charles, J. M. Duval *et al.*, Cryocoolers 12, Conference Proceedings edited by R. G. Ross Jr. (Kluwer Academic/Plenum Publishers, New York/USA, 2003) p.131.

Contact: jponcet@cea.fr


Theory and Simulat
Theory and Simula
Theory and Simulation
Theory and Simulation
Theory and Simu

BULLETIN
OF THE
DRFMC

Direction des Sciences de la Matière
CEA GRENOBLE

Theory and Simulation

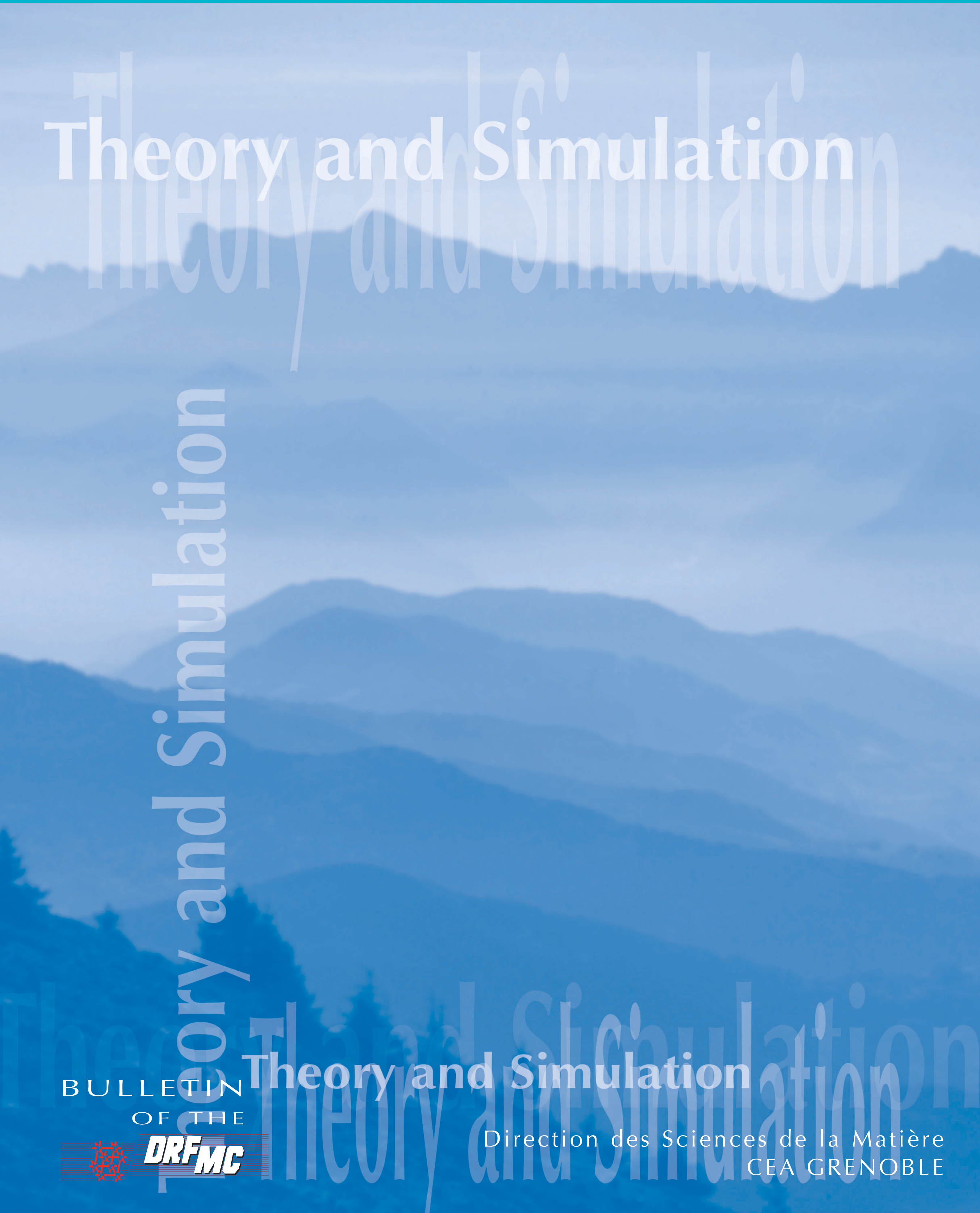

Theory and Simulation

BULLETIN
OF THE
DRFMC

Direction des Sciences de la Matière
CEA GRENOBLE